

Winter 2009

Infrared light activated floating micro stimulators for neuro-prosthetic applications

Kimberlyn M. Gray
Louisiana Tech University

Follow this and additional works at: <https://digitalcommons.latech.edu/dissertations>



Part of the [Biomedical Engineering and Bioengineering Commons](#)

Recommended Citation

Gray, Kimberlyn M., "" (2009). *Dissertation*. 472.
<https://digitalcommons.latech.edu/dissertations/472>

This Dissertation is brought to you for free and open access by the Graduate School at Louisiana Tech Digital Commons. It has been accepted for inclusion in Doctoral Dissertations by an authorized administrator of Louisiana Tech Digital Commons. For more information, please contact digitalcommons@latech.edu.

**INFRARED LIGHT ACTIVATED FLOATING
MICRO STIMULATORS FOR
NEURO-PROSTHETIC
APPLICATIONS**

by

Kimberlyn M. Gray, B.S.

A Dissertation Presented in Partial Fulfillment
of the Requirements for the Degree
Doctor of Philosophy

COLLEGE OF ENGINEERING AND SCIENCE
LOUISIANA TECH UNIVERSITY

March 2009

UMI Number: 3351359

INFORMATION TO USERS

The quality of this reproduction is dependent upon the quality of the copy submitted. Broken or indistinct print, colored or poor quality illustrations and photographs, print bleed-through, substandard margins, and improper alignment can adversely affect reproduction.

In the unlikely event that the author did not send a complete manuscript and there are missing pages, these will be noted. Also, if unauthorized copyright material had to be removed, a note will indicate the deletion.

UMI[®]

UMI Microform 3351359

Copyright 2009 by ProQuest LLC.

All rights reserved. This microform edition is protected against unauthorized copying under Title 17, United States Code.

ProQuest LLC
789 E. Eisenhower Parkway
PO Box 1346
Ann Arbor, MI 48106-1346

LOUISIANA TECH UNIVERSITY

THE GRADUATE SCHOOL

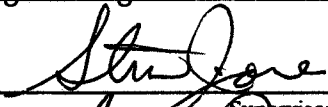

October 29, 2008

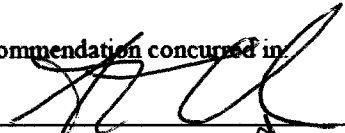
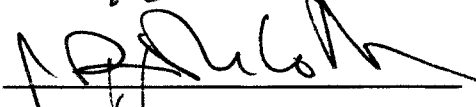
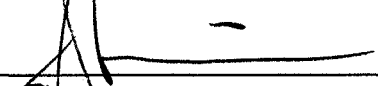
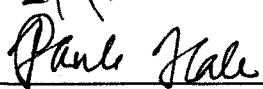
Date

We hereby recommend that the dissertation prepared under our supervision by Kimberlyn Gray


entitled Infrared Light Activated Floating Micro-Stimulators for
Neuro-Prosthetic Applications

be accepted in partial fulfillment of the requirements for the Degree of Doctor of Philosophy in Biomedical Engineering


Supervisor of Dissertation Research

Head of Department
Department

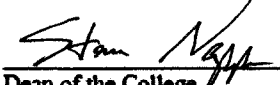
Recommendation concurred in





Advisory Committee

Approved:

Director of Graduate Studies

Approved:

Dean of the Graduate School


Dean of the College

ABSTRACT

The most common failures in neural stimulation implants are due to interconnect complications such as tissue response, lead migration, and lead breakages. The challenge in eliminating interconnects lies in minimizing device size to maintain spatial selectivity required in the CNS. One approach to this problem is a current generating device that can be stimulated by an external signal, such as light or sound. Here, we report the design, construction and testing of microphotodiode devices that can be stimulated remotely with near-infrared (NIR) light to generate current that can be injected locally into the peripheral nervous system. The use of near-infrared (NIR) light to activate microphotodiodes was investigated. The chip size of the prototype device is $300\mu\text{m}$ by $500\mu\text{m}$, and the small stimulation area necessitates a contact material capable of delivering a minimum charge injection rate of $0.5\text{ mC}/\text{cm}^2$. The charge transfer properties of iridium oxide, platinum, and titanium nitride were analyzed, and titanium nitride was found to have a stable charge injection rate above $0.5\text{ mC}/\text{cm}^2$. The volume conductor response of the diode showed a primarily capacitive transfer of energy into the tissue. Three diode geometries were implanted in a peripheral nerve, and an EMG signal was recorded in response to laser stimulation of two diode types. The diodes with the largest active area achieved successful stimulation despite size differences in contact area; this suggests the importance of active area size for stimulation. Further characterization of diode performance *in vivo* established an optimum pulse width for minimum light energy needed for diode activation. This optimum pulse width increased as implantation depth

increased. For an implantation depth of 3.5 mm, the energy threshold was 0.53 mJ/cm^2 which is 30 times below the maximum permissible exposure for $\lambda = 830 \text{ nm}$. The total energy required for stimulation at a given pulse width increased as tissue depth increased.

APPROVAL FOR SCHOLARLY DISSEMINATION

The author grants to the Prescott Memorial Library of Louisiana Tech University the right to reproduce, by appropriate methods, upon request, any or all portions of this Thesis. It is understood that "proper request" consists of the agreement, on the part of the requesting party, that said reproduction is for his personal use and that subsequent reproduction will not occur without written approval of the author of this Thesis. Further, any portions of the Thesis used in books, papers, and other works must be appropriately referenced to this Thesis.

Finally, the author of this Thesis reserves the right to publish freely, in the literature, at any time, any or all portions of this Thesis.

Author Alvin Buford Bony
Date 1-31-09

DEDICATION

*To my grandfather,
who taught me the value of learning,
and to Griffin who reminds me of all the joy in a normal day*

TABLE OF CONTENTS

ABSTRACT.....	iii
DEDICATION.....	vi
LIST OF TABLES.....	x
LIST OF FIGURES.....	xi
ACKNOWLEDGEMENTS.....	xiv
CHAPTER 1 INTRODUCTION.....	1
1.1 Deep Brain Stimulation.....	1
1.2 Hardware Complications in DBS.....	2
1.3 Effects of Motion.....	3
1.4 Eliminating the Effects of Tethering.....	4
CHAPTER 2 BACKGROUND.....	7
2.1 Optical Properties of Neural Tissue.....	7
2.2 Wireless Stimulation Devices.....	10
2.3 Injection of Charge into Neural Tissue.....	13
2.3.1 Capacitive Charge Injection.....	14
2.3.2 Faradic Charge Injection.....	15
2.3.3 Charge Storage Capacity.....	17

2.4 Electrode Materials	18
2.5 Biocompatibility	21
CHAPTER 3 METHODS	23
3.1 Fabrication of Micro-Photodiodes	23
3.2 Deposition of Contact Material.....	26
3.3 Volume Conductor Measurement.....	27
3.4 Determination of Laser Power	29
3.5 In Vivo Laser Power Threshold.....	30
3.5.1 Construction of Implant Device.....	30
3.5.2 Surgical Procedure	32
3.5.3 Modeling of In Vivo Data.....	33
3.6 In Vitro Testing of NIR Light.....	35
3.6.1 Experimental Setup.....	35
3.6.2 Construction of Holding Device	37
3.6.3 Preparation of Brain Tissue	38
3.6.4 Data Collection	39
CHAPTER 4 RESULTS	40
4.1 Volume Conductor Response of Photodiodes	40
4.1.1 Iridium Oxide.....	41
4.1.2 Platinum	43
4.1.3 Titanium Nitride.....	44
4.2 EMG Response to Microphotodiodes.....	49
4.3 Laser Power Curves	52

4.4 In Vivo Laser Power Threshold.....	54
4.5 NIR Light Propagation.....	60
CHAPTER 5 DISCUSSION.....	67
5.1 Volume Conductor Response of Photodiodes	67
5.2 EMG Response to Microphotodiodes.....	71
5.3 In Vivo Laser Power Threshold.....	72
5.4 NIR Light Propagation.....	75
CHAPTER 6 CONCLUSIONS AND FUTURE WORK.....	77
APPENDIX A CALCULATIONS FOR NIR SAFETY LIMITS	80
APPENDIX B PUBLICATIONS AND PRESENTATIONS.....	83
REFERENCES	85

LIST OF TABLES

Table 1	List of the 22 Types of Micro-photodiodes by Device Geometry.....	25
Table 2	ANOVA for the Stimulation Threshold Data Fit.....	56
Table 3	Parameter Testing for the Stimulation Threshold Data Fit.....	56
Table 4	ANOVA of 2 nd -order Model Valid for $d \leq 0$	63
Table 5	Parameter Test of Piecewise 2 nd -order Model Valid for $d < 0$	63
Table 6	ANOVA for the Spatial Light Propagation Data for $x_1 \geq 0$	64
Table 7	Parameter Testing for the Spatial Light Propagation Data Model Fit for $x_1 \geq 0$	64
Table 8	ANOVA for the Spatial Light Propagation Data for $x_1 < 0$	65
Table 9	Parameter Testing for the Spatial Light Propagation Data Model Fit for $x_1 < 0$	65
Table 10	Symbols and Values Used in NIR Safety Limit Calculation.....	81

LIST OF FIGURES

Figure 1	Penetration depth of NIR light in grey (top) and white (bottom) matter [20]....	8
Figure 2	Relative levels of reflection (R), absorption (K), and scattering (S) for different tissue types [20].	8
Figure 3	Schematic of a single photovoltaic element of a retinal prosthesis array design.....	12
Figure 4	The electrode-electrolyte interface between an electrode composed of metal atoms C and an electrolyte containing ions C^+ and anions A^- of the electrode metal [28].	15
Figure 5	Circuit model of the electrode-electrolyte interface.	17
Figure 6	Electrical response of individual photodiodes in a microphotodiode array to an IR stimulus 25].....	21
Figure 7	The current generated by a microphotodiode array in response to an IR stimulus[6].....	21
Figure 8	The interdigitated design of the p+/n+ devices.	24
Figure 9	Cross section of the fabrication layers of the photodiode device.....	24
Figure 10	The layout of the leakage resistor in the micro-photodiodes.	26
Figure 11	Diagram of volume conductor measurements.....	28
Figure 12	Diagram of laser power measurement setup.	29
Figure 13	Device used to determine the implantation depth.	31
Figure 14	Block diagram of light loss experiments.	31
Figure 15	Linearizable functions used to select a transform [51].....	34
Figure 16	General setup used to measure the spatial resolution of NIR light through grey matter.	36

Figure 17	The setup of the 100 μm receiving fiber and tissue sample.	36
Figure 18	Slit used in light propagation experiments.	37
Figure 19	Location of brain tissue sample.	38
Figure 20	The movement of the light source in relation to the tissue sample and receiving fiber.	39
Figure 21	The geometric layout of diode types 19 and 22.	40
Figure 22	The voltage generated on the surface of the IrOx cathode of diode type 22 in the volume conductor.	42
Figure 23	The voltage generated in the volume conductor just above the surface of the IrOx cathode of diode type 22 during the first 200 μs of the laser pulse.	43
Figure 24	The voltage generated in the volume conductor just above the surface the Pt cathode of diode type 22 during the first 200 μs of the laser pulse.	44
Figure 25	The voltage generated on the surface of the TiN cathode of diode type 1 in the volume conductor.	45
Figure 26	The voltage generated in the volume conductor just above the surface of the TiN cathode of diode type 1 during the first 200 μs of the laser pulse	46
Figure 27	The voltage generated in the volume conductor just above the surface of the TiN cathode of diode type 15 during the first 200 μs of the laser pulse ...	47
Figure 28	The voltage generated in the volume conductor just above the surface of the TiN cathode of diode type 18 during the first 200 μs of the laser pulse ...	48
Figure 29	The voltage generated in the volume conductor just above the surface of the TiN cathode of diode type 19 during the first 200 μs of the laser pulse	49
Figure 30	The EMG response of the calf muscle of a rat in response to a single pulse laser stimulation of a photodiode implanted into the sciatic nerve	50
Figure 31	The EMG response of the calf muscle of a rat in response to laser stimulation of a photodiode implanted into the sciatic nerve, repeated with a frequency of 10 Hz.	51
Figure 32	The EMG response of the calf muscle of a rat in response to laser stimulation of a photodiode implanted into the sciatic nerve, repeated with a frequency of 50 Hz.	52

Figure 33 Part A shows the square wave input to the laser Part B show the voltage generated across a 3.8Ω resistor by the Optek OPF480.....	53
Figure 34 Power curve fit of the Lasiris laser.....	54
Figure 35 Laser power stimulation thresholds for diode type 18 for four thicknesses of neural tissue.....	55
Figure 36 Laser power stimulation thresholds for diode type 19 for four thicknesses of neural tissue.....	55
Figure 37 The power needed for stimulation for diode 19 at 0.5 mm vs. the power predicted by the model.	57
Figure 38 Minimum pulse width for stimulation at each depth.....	58
Figure 39 Optimum pulse width for stimulation at each depth.	59
Figure 40 Power threshold at $PW = 200 \mu s$	60
Figure 41 NIR light propagation horizontally through the saline.....	61
Figure 42 NIR light propagation horizontally through the brain tissue.....	61
Figure 43 NIR light propagation at 0.5 mm thickness.....	62
Figure 44 NIR light propagation at 1.25 mm thickness.....	62
Figure 45 The predicted transmission at $\lambda = 830 \text{ nm}$ through brain tissue for the spatial propagation model	66
Figure 46 Comparison of the experimental data to the predicted transmission for the spatial propagation model at $\lambda = 830 \text{ nm}$ at a tissue thickness of 0.5 mm.....	66
Figure 47 Volume conductor voltage measurements at $z = 0, 20, \text{ and } 40 \mu m$ above the cathode of a Pt photodiode.	70
Figure 48 Pulse train measurements of a Pt diode with the recording electrode A) touching the contact and B) just above the surface of the contact at $z = 0 \mu m$	71

ACKNOWLEDGEMENTS

For their advice and assistance, I would like to thank the members of my committee: Dr. Steven A. Jones, Dr. Paul N. Hale, Dr. Stan Cronk, Dr. Mark DeCoster, and Dr. Alan Chiu. I would especially like to thank Dr. Jones for his feedback and insight on my dissertation research and his suggestions for the improvement of the final product. I would like to thank Dr. Hale for his support through the final stages of my research.

I would like to thank Dr. Stan Napper for his guidance and support throughout my academic career. I would also like to thank Dr. James Spaulding for teaching me proper animal handling and protocol. For the supervision of experiments, I would like to thank Dr. Walter Besio. For the loan of equipment to complete my experiments, I would like to thank Dr. David Mills. I would like to thank Dr. Raja Nassar for his instruction and advice on statistical models.

I would like to thank Scott Morstatt for his patience and willingness to discuss at length the appropriate tools and materials I needed to construct my prototypes. I would like to thank Celia Wall for teaching a young graduate student the ropes. I would also like to thank Regina Foster for helping me through my numerous difficulties with acquiring journals.

I would like to thank the members of the Neural Sensing and Modulation Lab for their advice, support, and help finding the best setup for various projects. Finally, I would

like to thank my dearest friend, Dr. Marcia Pool, for her unfailing encouragement, her help with my experiments, and her willingness to review my work and to offer her advice.

CHAPTER 1

INTRODUCTION

Electrical activation of the peripheral and central nervous system has been used to treat neural disorders for many decades. Well-known devices that are based on this concept include cochlear prostheses, deep brain stimulators for Parkinson's disease, dorsal spinal cord stimulators for chronic back pain, sacral root stimulators for bladder and bowel control in spinal cord injury patients, and vagus nerve stimulators for epilepsy patients. Such devices are being implanted in thousands of patients every year. One of the factors limiting additional applications for neural stimulation is the mechanical stress on the electrode interconnects. These stresses cause complications such as lead breakage, electrode migration, erosion, and tissue damage [1]. These problems will be illustrated below in the context of deep brain stimulation.

1.1 Deep Brain Stimulation

Deep Brain Stimulation (DBS) for the treatment of mobility disorders was introduced by Benabid et al. in 1987 [2]. Initially, stimulation of the thalamus was approved for the treatment of essential tremor and Parkinson's disease. Stimulation of the subthalamic nucleus and the global pallidus for the treatment of Parkinson's disease was then approved. DBS has been used to treat tremor associated with multiple sclerosis and dystonia [3] and for non-movement disorders such as epilepsy and pain [1]. DBS of the

periventricular grey matter in the mesencephalic transition area, the internal capsule, and the motor cortex have all been used to treat chronic pain [4, 5].

A DBS system consists of one or more stimulating electrodes that are implanted directly into the brain. The electrodes are connected to a thin insulated wire that extends through the brain to an opening in the skull (burr hole) where the wire is attached to an extension cable. The extension cable is also a thin insulated wire that is threaded through the skin of the head and neck into the upper chest region, where it is connected to a neurostimulator implanted under the skin. Despite the benefits of DBS, hardware complications, such as lead fracture, migration, and erosion, have ranged from 6.7—27% in recent studies [3, 6-9].

1.2 Hardware Complications in DBS

Studies have shown that 34.7% to 50% of hardware complications in DBS are lead fractures [3, 7-8]. The fractures occur at either the connection of the lead to the stimulator or at the burr hole connection of the lead and the extension cable. Patients with essential tremor, dystonia, or dyskinesia are most likely to experience lead fracture [1, 8]. The rate of lead fractures in these patients can be reduced by moving the connector of the lead and extension cable from below the mastoid in the neck to a location near the burr hole on the calvarium [7-8]. In patients with Parkinson's disease, lead damage most often occurred after a fall [6]. Blomstedt et al. reports an average time of 25 months for lead failure cases [8]. In all cases of fracture, further surgery was required to remove and replace the failed lead.

Lead migration, the shifting of the connection to the electrode, accounts for 4.3% to 20% of hardware complications in DBS [1, 3, 8]. This motion of the connectors causes

a shift in the position of the stimulating electrode, which reduces the effect of the stimulation [3]. Most common in movement disorder patients, lead migration is caused by the forces on the lead resulting from motion and is a contributing factor to lead fracture [1, 8]. Patients need a surgery to reposition the electrode and restore control of symptoms.

Lead erosion is the cause of lead failure in 12.5 % of hardware complications [7]. A study of leads used in cardiac pacemakers shows a breakdown of the inner insulation of the lead, made of polyether polyurethane, but intact outer silicone rubber insulation layer. Pitting and cracking were observed in localized areas of the inner layer, with the damage beginning on the exterior of the insulation and working inward. The worst erosion occurred in areas of high strain due to repeated movement [10]. Eventually, erosion leads to lead failure and the return of patient symptoms, requiring surgery to replace the damaged lead.

1.3 Effects of Motion

In DBS, the relative motion of the interconnects to the brain tissue—micromotion—damages both the electrode interconnects and the surrounding neural tissue [11-12]. Physiological sources of micromotion include volume changes caused by the cardiac rhythm and pressure changes in the cerebrospinal fluid caused by respiration. Respiration causes low frequency, relatively large displacements of $\sim 30\ \mu\text{m}$, and the cardiac rhythm causes higher frequency, small displacements of $\sim 1\text{-}4\ \mu\text{m}$. Behavioral sources of micromotion are head and trunk movements. Small head motions can damage the surrounding neural tissue, which can increase stimulation thresholds. Damage to the stimulation device can be caused by large acceleration as seen from a sneeze or fall.

Finally, micromotion is caused by mechanical sources such as external vibration of the implant that translates to the electrode through the lead wires [12-13]. This micromotion intensifies the mechanical mismatch of the neural tissue and the electrode materials [14]. Micromotion in the CNS causes the same problems as with stimulation implants in the Peripheral Nervous System (PNS). In the PNS, the motion of the surrounding muscles and the flexibility and movement of the nerves induce large mechanical stresses and strains on the interconnects, triggering lead breakage [15].

The tissue reaction to an implant changes the electrical properties of the tissue around the implant [14]. There is an initial inflammation due to the implantation of the device, followed by the formation of a sheath of astrocytes and microglia on the surface of the implant. Brain stimulation devices tethered to the skull cause more tissue reaction than “free floating” devices [16]. The micromotion of the implant kills otherwise healthy cells around the implant [17].

1.4 Eliminating the Effects of Tethering

Attempts to minimize the tethering forces on implants include developing small diameter, flexible wires for use as interconnects [18]. Subbaroyan et al. show that a flexible wire decreases the force transferred along the interconnect from the tethering point to the implanted device. However, the flexibility increases the difficulty of accurate implantation for the control of symptoms. The strain on the connection point at the skull is also increased, leading to a higher chance of lead fracture and erosion [14].

One design in development to eliminate tethering is a Radio Frequency (RF) controlled microstimulator [19]. The device has an onboard power supply and receiving antennae causing the cylindrical device size is a few millimeters long and two millimeters

in diameter. Because this device is relatively large compared to neural structures, it is designed to be implanted into muscles for stimulation. One way of solving this mechanical mismatch and tethering problem is to place telemetry electronics into the stimulator and control it transcutaneously with an extra-corporal magnetic coil and electronics, thus eliminating the interconnects. However, because these devices contain telemetry and power circuitry, they are large (a cylinder of 2-2.5 mm in diameter and 10-16 mm in length) compared to the neural structures to be activated. Thus, spatial selectivity is poor and can be used only for activation of the whole peripheral nerves or muscles. The next generation of electrical stimulation devices should be in the micrometer size range, selectively addressed, activated remotely without wires attached, and targeted for specific nerve cell types in the nervous system. The proposed Floating-Light-Activated-Micro-Electro-Stimulators (FLAMES) will have all the features of the next generation stimulators. These devices are micro scale photovoltaic elements, anticipated to be smaller than $50 \times 50 \mu\text{m}^2$, that are activated by light energy at Near InfraRed (NIR) wavelengths. Many of these devices will be implanted into the target area, such as inside the fascicles of a peripheral nerve or into the grey or white matter of the spinal cord or brain. The devices will be selectively activated by an array of NIR light emitting diodes placed extraneurally or extradurally. Spatial selectivity will be provided by focusing the NIR beam at specific micro-stimulators.

The purpose of this work is to develop and test the efficacy of a wireless microstimulator for use in the central nervous system. To this end, three sets of NIR microphotodiodes with 22 distinct geometries were fabricated. Three electrode interface materials—iridium oxide, platinum, and titanium nitride—were deposited on the

photodiode contacts. The voltage generated by these devices in response to a laser pulse was measured in a volume conductor with a specific resistivity similar to that of nervous tissue. Selected photodiodes were implanted into the sciatic nerve of Sprague-Dawley rats to determine if the diode was capable of stimulating a nerve. EMG response to a laser stimulation of an implanted photodiode was measured; this EMG response indicated successful neural stimulation. The successful photodiodes were then implanted at selected depths in the sciatic nerve. The power threshold required for stimulation was established across a range of pulse widths. Using the power threshold data, a statistical model was designed to predict the laser power required for stimulation at selected implantation depths and stimulation pulse widths.

A second set of experiments was conducted to study the spatial resolution of NIR light through neural tissue and determine the minimum separation distance between photodiodes. The intensity of light transmitted through a slice of rat brain tissue was measured as the light source was moved incrementally away from the receiving optical fiber under the tissue. These tests were repeated for increasing thickness of tissue, and a statistical model was developed to predict the percent of power collected under the tissue as the distance between the light source and receiving fiber was increased. This model was used to help determine the significance of the variables tested.

CHAPTER 2

BACKGROUND

2.1 Optical Properties of Neural Tissue

In order to use optically activated photovoltaic devices as microstimulators for either the CNS or PNS, the light power from a laser source must be able to penetrate through the tissue to the implant. Four optical properties which together determine the penetration depth of a wavelength of light are reflection, absorption, scattering, and transmission. Penetration depth is defined as the depth of tissue at which the optical power is 37% of the initial optical power [20]. The two most important factors in determining penetration depth for light are absorption and scattering. For biological tissue, the maximum penetration depth is achieved by using NIR light with wavelengths from 650-950 nm.

Figure 1 shows the penetration depth of wavelengths from 360—900 nm. Penetration depth increases significantly from 600-900 nm but is much higher in grey matter than white matter [20]. Figure 2 compares the contributions of absorption, scattering and reflection as a function of wavelength, and shows that reflection and scattering become the dominant causes of signal loss for larger wavelengths, while absorption is the least dominate property for wavelengths between 600 and 900 nm [20]. A large portion of the light is reflected before entering the tissue and much of the light entering the tissue is scattered.

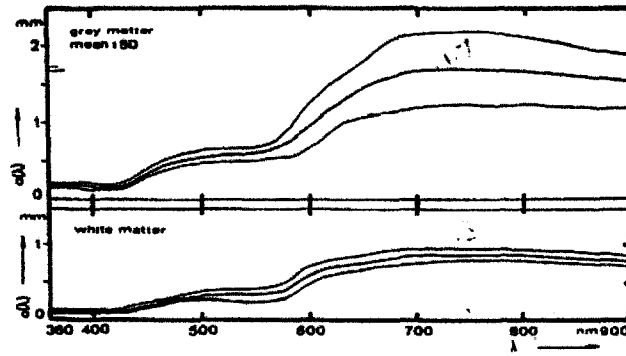


Figure 1 Penetration depth of NIR light in grey (top) and white (bottom) matter [20].

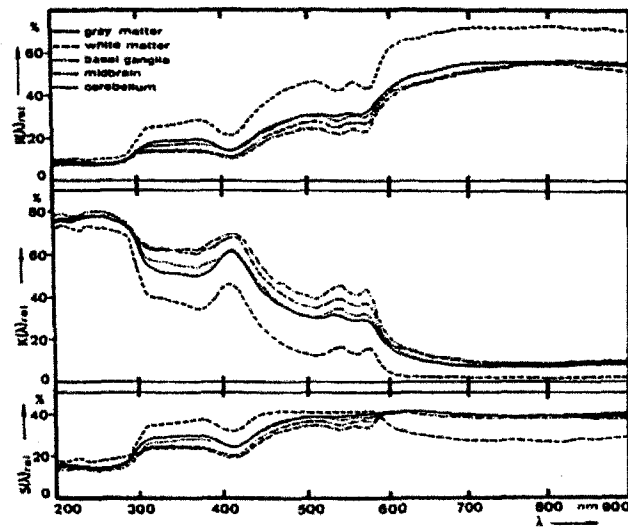


Figure 2 Relative levels of reflection (R), absorption (K), and scattering (S) for different tissue types [20].

The Lambert-Bouguer Law states that all layers of material absorb the same fraction of incident light shining on them. Equation 2.1 expresses the probability that a photon of light over a path will be absorbed. This law can be expressed in the form:

$$\frac{dI}{I} = -\mu_a dz, \quad \text{Equation 2.1}$$

where

$\frac{dI}{I}$ = fraction of incident light,

$-\mu_a$ = absorption coefficient (mm^{-1}),

dz = thickness (mm).

Equation 2.2 can be used to determine the intensity of light transmitted to a certain depth in the tissue

$$I(z) = I_0 e^{-\mu_a z}, \quad \text{Equation 2.2}$$

where

I = transmitted light intensity at depth z ,

I_0 = initial light intensity,

z = depth (mm).

The absorption coefficient is the probability that a photon will be absorbed by the tissue. The absorption pathlength, $1/\mu_a$, is the path a photon travels between absorption events. The depth of laser penetration can be determined by finding the optical density of the tissue with Equations 2.3 and 2.4

$$OD = \log\left(\frac{1}{T}\right), \quad \text{Equation 2.3}$$

$$T = \frac{I}{I_0}, \quad \text{Equation 2.4}$$

where T is defined as the ratio of transmitted light power to incident light power [21].

The attenuation of light in tissue at NIR wavelengths is only partially determined by absorption. The majority of the attenuation is due to light scattering caused by changes in refractive index at the microscopic level. Light can be back scattered and exit the tissue through the initial entry point or forward scattered and measured with the light transmitted through the tissue. The amount of light transmitted through the tissue can be determined by Equation 2.5

$$I(z) = I_0 e^{-\mu_s z}, \quad \text{Equation 2.5}$$

where μ_s is the scattering coefficient, which gives the probability that a photon will be scattered in the tissue [21].

Because total attenuation in the tissue is determined through both absorption and scattering in the tissue, the intensity of light transmitted through tissue is shown in Equations 2.6 and 2.7:

$$I(z) = I_0 e^{-\gamma z}, \quad \text{Equation 2.6}$$

where

$$\gamma = \mu_a + \mu_s. \quad \text{Equation 2.7}$$

NIR light is non-ionizing, so the primary safety concern for NIR light is heating of the tissue [22]. Scattering, dominant in attenuation, has no effect in the heating of the tissue due to light.

2.2 Wireless Stimulation Devices

Numerous retinal disorders can lead to the slow loss of vision and eventually cause complete blindness. Retinitis Pigmentosa (RP) affects an estimated 1 in 3000 people [23]. RP is a group of hereditary disorders that cause a breakdown of the function of both types of photoreceptors in the retina. Macular degeneration, the leading cause of

vision loss in people over fifty-five, is caused by the loss of function of the photoreceptors known as cones. The number of people affected by macular degeneration is increasing as the population increases in age. Early symptoms of these retinal disorders include night blindness, slow light-to-dark adaptation, and progressive tunnel vision. The disease slowly progresses over time, but usually accelerates when the patient approaches thirty or forty years old until the patient is completely blind [24]. Transplants of healthy retinal tissue have been shown to survive *in vivo* but have failed to show restoration of visual function. Electrical stimulation of the retina induces visual impressions in both normal patients and those who are blind from RP [25]. Reproducible visual potentials were evoked in normal animal subjects with similar electrical stimulation [23].

Photovoltaic elements have been built by other groups to stimulate the retinal cells of cats and rabbits with light energy of 880 nm in a test of a neural prosthetic concept [23, 36-27]. Schlosshauer's group in Germany has successfully demonstrated that a 3 mm diameter device with 7000 photovoltaic elements each with a dice area of $20 \times 20 \mu\text{m}^2$ can generate currents as high as 300 μA when about 200 μA current is pulsed through NIR LED source. The large array of photodiodes replaces the lost photoreceptors but utilizes the underlying nerves. This group has recorded electroretinogram signals from the implanted eye of a rabbit indicating that the implant was able to activate subretinal cells when illuminated by NIR light sources. Shown in Figure 3, each individual element has a cathode area of $8 \times 8 \mu\text{m}^2$ with the anode located across the bottom of the device. The diodes are intended to respond to visible wavelengths, but are currently tested at 880 nm to isolate photodiode response from the response of the remaining photoreceptors [26].

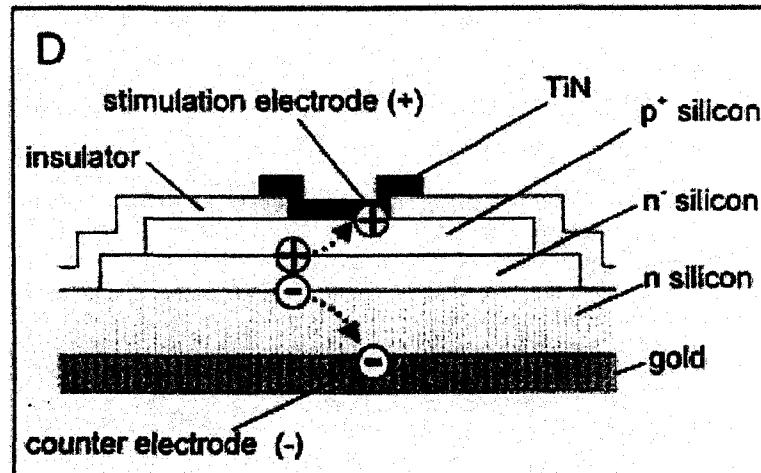


Figure 3 Schematic of a single photovoltaic element of a retinal prosthesis array design.

In their design, each element with a contact area of $8 \times 8 \mu\text{m}^2$ supplied about 42 nA. This is substantially larger than the transmembrane current of a medium size axon ($\sim 10 \mu\text{m}$ diameter) at a node of Ranvier, which is in the order of 3-4 nA. Most of the stimulator current will spread into the extracellular medium and not go through the cell membrane. Thus, the current and potential distribution around the device was estimated using the finite element modeling package TCAD to determine the minimum dice area for the device sufficient to stimulate a nerve soma or axon within a volume of $100 \mu\text{m}$ distance from the cathodic end of the device. Because a substantial amount of NIR light energy will be reflected in the white (70%) and grey (55%) matters of the neural tissue within the 700-990 nm range, each contact area is expected to be larger than $8 \times 8 \mu\text{m}^2$ to reduce the internal resistance and increase the voltage generated. However, the active area of the photodiode is expected to be smaller than $50 \times 50 \mu\text{m}^2$.

Peachey and Chow have designed a similar microphotodiode array 2 mm in diameter with an individual diode measuring $20 \times 20 \mu\text{m}^2$. These devices respond to wavelengths from 500 to 1100 nm. The group has tested the use of gold, platinum, and

iridium as contact materials and discovered gold did not transfer enough charge to be useful. The device thickness has been reduced to 50 μm to minimize damage to the surrounding tissues [25]. In contrast to the array approach, the devices produced in this study are single photodiodes intended to stimulate a distinct structure in the CNS.

In this project, a Neurocal simulation was used to determine the current needed to activate action potentials in the neuron. Neurocal simulates neural activity and stimulation by solving the cable equation. A neuron at 37 $^{\circ}\text{C}$ with one axon (diameter = 10 μm) and two dendrites was modeled with one external stimulator. The neuron was divided into 55 segments with the external stimulation (a square wave) placed at segment 27 in the middle of the neuron but placed 100 μm from the center of the neuron.

Early testing of the photodiode in a volume conductor with resistivity of 300 $\Omega\text{-cm}$ showed that the voltage produced in the volume declines as the distance from the photodiode contact increases. One hundred micrometers was chosen as a distance where significant voltage is still experimentally produced in the volume. Neurocal simulation revealed that current threshold values varied more with changes in pulse width than with changes in distance from the axon. Therefore, distance from the axon was kept constant throughout the simulation. Decreasing this distance would result in lower current thresholds and higher penetration depths through the tissue.

2.3 Injection of Charge into Neural Tissue

To achieve neural stimulation, electrical charge must be injected into neural tissue by metal electrodes. However, charge is carried by electrons in metal electrodes but by ions in physiological tissues. The meeting of electrode and tissue is known as the electrode-electrolyte interface. Two mechanisms allow charge to be transferred into the

tissue at the electrode-electrolyte interface: capacitive and faradic. The dominant mechanism of transfer is determined by the electrode material.

2.3.1 Capacitive Charge Injection

In capacitive charge transfer, there is no transfer of electrons across the electrode-electrolyte interface. Metal ions in the tissue combine with the metal electrode, leading to a double layer of charge on the surface of the electrode because of the opposing charges on the electrode surface and the tissue. A layer of water molecules forms between the two layers of charge and acts as a dielectric capacitor [28]. If only capacitive charge transfer occurs, the interface can be modeled as a double layer capacitor C_{dl} , shown in Equation 2.8

$$C_{dl} = \epsilon\epsilon_0 \frac{rA}{t}, \quad \text{Equation 2.8}$$

where

C_{dl} = double layer capacitance,

ϵ = dielectric constant of the material,

ϵ_0 = dielectric permittivity of a vacuum,

r = ratio of real to geometric surface area,

A = geometric surface area, and

t = distance between layers.

During stimulation, the charge built up on the surface of the electrode changes, causing a change in the charge in the electrolyte. When current is injected through the negative electrode, the surface of the electrode builds up negative charge. The electrode surface now attracts cations and repels anions in the electrolyte. The counter electrode

acts as the positive electrode which repels cations and attracts anions. Figure 4 shows the exchange of charge at the interface where ions are formed in the double layer of charge and injected into the tissue. This mechanism of injection is ideal because no electrochemical reactions occur to cause changes in the tissue [29].

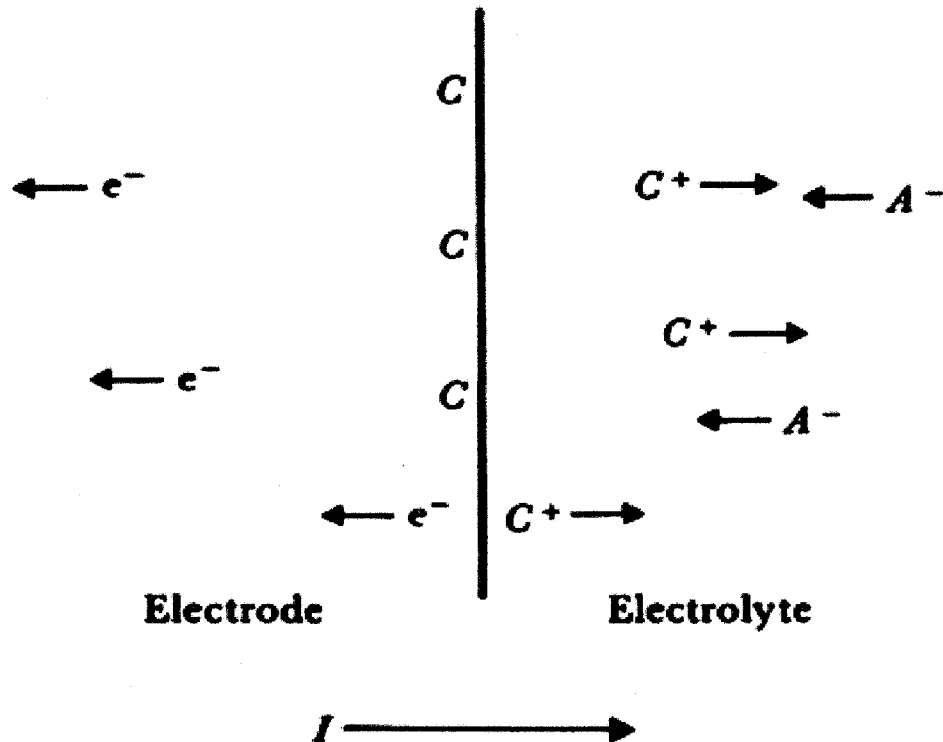


Figure 4 The electrode-electrolyte interface between an electrode composed of metal atoms C and an electrolyte containing ions C^+ and anions A^- of the electrode metal [28].

2.3.2 Faradic Charge Injection

In faradic charge injection, electrons cross the electrode-electrolyte interface through a chemical species being oxidized or reduced. At the negative interface, the ions are reduced and gain an electron. Ions at the positive interface are oxidized and lose an electron. The faradic mechanism injects a much higher charge into the neural tissue because a higher level of charge is necessary for the oxidation/reduction process.

However, the ability to inject more charge must be balanced by the injection of new chemical ions into the tissue. The injection process can be labeled as reversible or irreversible. If the reaction is reversible, the new species introduced into the tissue by oxidation is removed by reduction when a current is applied in the opposite direction, and no net changes occur in the tissue. Once the reaction becomes irreversible, the introduced species begin to build up in the tissue, leading to changes and damage. An example of a reversible reaction can be seen with an electrode made of Iridium (Ir) as shown in Equation 2.9,



Reversible reactions can be pushed into irreversible reactions by increasing the current levels beyond set limits. These limits are determined by the electrode material and stimulation protocols.

Real world electrodes contain both capacitive and faradic processes. Figure 5 shows a simple electrical circuit model of charge transfer across the electrode-electrolyte interface. The double layer capacitance, C_{dl} , represents the capacitive charge transfer, and the parallel faradic impedance, R_d , represents the charge transferred with electrons exchanged between the electrode and electrolyte. The value of the impedance and capacitance is dependent on the electrode material and the electrolyte.

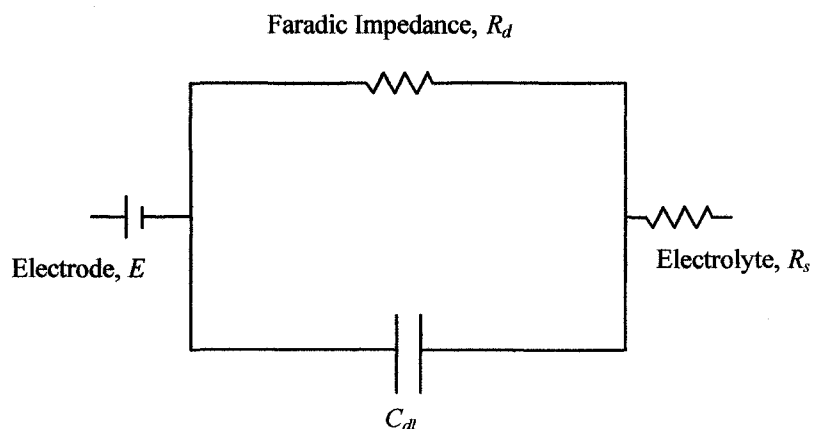


Figure 5 Circuit model of the electrode-electrolyte interface.

The interface behaves as a low pass filter, making the electrode impedance frequency dependent. Impedance is highest at low stimulation frequencies because R_d adds in series with R_s . When stimulation frequencies are high, the effect of R_d on the electrode impedance is lowered, and the impedance approaches R_s . The electrode impedance and capacitance are also dependent on current density, with R_d decreasing and C_{dl} increasing as current density increases [30]. As overall impedance decreases, the ease of charge transfer across the interface increases [31], which increases signal gain [32].

2.3.3 Charge Storage Capacity

As the capacitance increases in the double layer of charge, so does the Charge Storage Capacity (CSC) of the electrode. The CSC is the amount of charge stored in the double layer capacitance and reversible faradic reactions of the electrode for injection into the tissue [29]. An electrode with a high CSC can inject more charge into the tissue than an electrode with a low CSC. If a charge higher than the CSC builds up on the electrode surface, a dielectric breakdown will occur and cause irreversible reactions within the tissue. Electrode materials that have been or can be deposited with a rough

surface area to increase the real surface area without increases the geometric surface area of a diode. The capacitance can then be calculated from Equation 2.8. This allows for an increase in the capacitance and the CSC of the electrode without increasing the geometric surface area of the electrode. Increasing real surface area while minimizing geometric electrode size is important to minimize tissue damage from the electrode [33].

2.4 Electrode Materials

An electrode used in neural stimulation must transfer a large charge into the tissue in high frequency, low pulse width situations. This high charge must be delivered without causing irreversible reactions such as electrode corrosion, electrode dissolution, gas bubbling, or toxic chemical creation. The impedance of the electrode should be low enough to allow for a high charge injection limit. The charge injection limit is the amount of charge that the electrode can inject into the tissue during stimulation and is usually lower than the CSC because an electrode can store more charge than it can transfer. The charge injection limit depends on electrode material, surface structure, and stimulation protocols. To avoid damage to the electrode or the surrounding tissue, stimulation must occur through either capacitive or reversible faradic reactions. Stimulation density must occur below the 1 mC/cm² neural damage limit [34] but above the 0.5 mC/cm² stimulation threshold in small area electrodes [35].

Platinum (Pt) and platinum-iridium alloys are frequently used in electrical stimulation because of their resistance to corrosion and electrical properties. Pt has been used in long term stimulation in cochlear implants and has a proven record of biocompatibility. The safe charge injection limit of Pt is 400 $\mu\text{C}/\text{cm}^2$ [36], which is well under the safety limits for charge injection into neural tissue. Pt is a soft metal, and is

often alloyed with iridium (Ir) to improve the mechanical strength. These 10-30% alloys have charge injection limits similar to pure Pt [37]. Erosion of Pt-Ir electrodes has been shown during stimulation with charge densities as low as 200 - 400 $\mu\text{C}/\text{cm}^2$, and both Pt and Ir were found in tissue adjacent to the electrode tip [38]. Because of its low charge injection limit, Pt may not be a good choice for neural stimulation with very small area electrodes. To increase the CSC and lower the impedance of a Pt electrode, a layer of platinum black may be deposited on the surface. However, Pt black is easily removed by insertion into muscle or neural tissue and deteriorates during stimulation, making it unsuitable for long term applications [33].

Another material considered for use in neural stimulation is Iridium Oxide (IrOx). IrOx is a porous, multi-layer oxide film that can be formed on the surface of an Ir electrode through a process known as activation. In IrOx activation, a current is applied to the electrode while it is bathed in a solution containing Ir. The majority of charge transfer in an IrOx electrode is due to reversible faradic reactions [39]. The oxidation/reduction reactions of the IrOx layers, unlike Pt, do not produce components soluble in the electrolyte [35]. The total amount of available charge is determined by the activation process and thickness of the IrOx layer. IrOx electrodes have a CSC as high as 30 mC/cm^2 but have a charge injection limit of 3-4 mC/cm^2 [40-41]. IrOx electrodes have proven stable at charge densities under 3.2 mC/cm^2 [38], and though the CSC decreased with chronic pulsing over 5 days, the injected charge remained sufficient for stimulation [39]. Studies using IrOx as a cortical implant have shown it to be biocompatible [34, 39].

Titanium Nitride (TiN) coatings are frequently used in cardiac pacing and could prove useful in neural stimulation [42]. The mechanism of charge injection in TiN

electrodes is capacitive, which often results in low charge injection limits. However, the sputter deposition of TiN results in a porous, columnar, high surface area coating [43-44]. This high surface area results in charge injection limits of 1 mC/cm^2 for a pulse less than 0.5 ms and ranging from 2.2-3.5 mC/cm^2 for a pulse of 1 ms [43, 45]. Unlike Pt and IrOx, sputter deposition of TiN is a common micromanufacturing process so special deposition procedures are not required [41]. Hammerle et al. demonstrated that TiN microelectrodes arrays are functional after 16 months of continuous use in vitro although the decay time increased over the same period [46]. The biocompatibility of TiN has been debated. In one study, the exposure of TiN to a cell culture resulted in a higher percent of cell death than the control [47]. However, Schlosshauer et al. found that the cell attachment to the surface of TiN was low and the quantity of cell death due to exposure to TiN was similar to that of the controlled cell culture [26]. The biocompatibility of TiN may depend on the system it is implanted in [48-49].

Peachey and Chow have measured the response of Au, Pt, and IrOx coated microphotodiode arrays. Figure 6 show the response of 3 different photodiodes to a 100 ms IR pulse. Both Au and Pt have a capacitive response with a sharp peak and rapid return to the baseline, significantly before the end of the stimulus. The IrOx photodiode has a much slower decay and a dc component representing a faradic response. The faradic response transfers an increased quantity of charge into the tissue, improving the chances of stimulation. Both the Pt and IrOx coated photodiodes were shown to stimulate the nerves in the subretinal space [25].

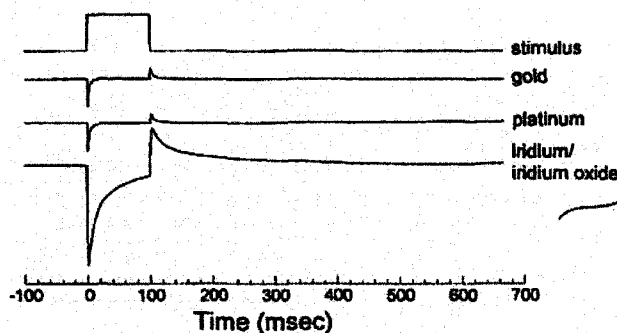


Figure 6 Electrical response of individual photodiodes in a microphotodiode array to an IR stimulus [25].

Figure 7 shows the response of a TiN coated microphotodiode array designed by Schlosshauer et al. [26]. The initial peak has a slow decay, but little voltage elevation at the end of the pulse indicating the expected capacitive response. The peak current averaged $300 \mu\text{A}$ for a $50 \text{ mW}/\text{cm}^2$ stimulus and was dependent on the power of the LED stimulus.

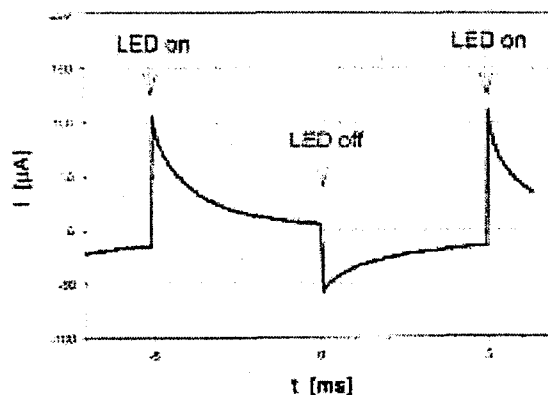


Figure 7 The current generated by a microphotodiode array in response to an IR stimulus [26].

2.5 Biocompatibility

Survival of the retinal glia and neurons was tested on silicon dioxide (SiO_2), silicon nitride (Si_3N_4), and Ir surfaces in cultures. There were no significant differences in

the survival rates between retinal cells planted on these materials and the control group planted on glass cover slips for four weeks of incubation time [47]. The number of surviving cells was markedly reduced on titanium nitride (TiN) surfaces, although the effect was not mediated by diffusible factors released from the material. Cell adherence to plastic, SiO₂, and Ir surfaces was only about 20% of the originally plated cells after 6 hours of culture. Plating the surfaces with poly-D-lysine/laminin (PDL), poly-L-lysine/laminin (PLL) or laminin increased the cell adherence up to 80% at the end of the incubation times as long as three weeks. Schlosshauer et al. (1999) confirmed that bare TiN and SiO₂ do not permit cell attachment. They treated the surface of photovoltaic elements with oxygen plasma under high voltage to render the surface hydrophilic and coated them with a double layer of PDL. In a 3 day incubation time, the cell adhesion remained stable allowing even cell proliferation as deduced from an increase in cell population [26]. In conclusion, SiO₂ seems to be biocompatible and to allow the survival of cells in cultures, although its surface is not hydrophilic and thus prevents cell attachment. Cell attachment can also be achieved for both SiO₂ and TiN materials by coating their surface with materials like PDL.

CHAPTER 3

METHODS

3.1 Fabrication of Micro-Photodiodes

The micro-photodiodes studied in this work were designed at the Optical Characterization and Nanophotonics Laboratory, Electrical Engineering, Boston University and fabricated at Ecole Polytechnique Fédérale de Lausanne (EPFL) in Switzerland. Silicon (Si) lithography and processing techniques were followed using Si as the semiconductor. An anti-reflection coating was deposited over the active area, and aluminum metallization formed the rectangular contacts. Ion implantation was used to form highly doped positive (p+) and highly doped negative (n+) regions within the substrate. An interdigitated p+/n+ design, shown in Figure 8, limited the maximum distance between the p+ and n+ regions to 20 μm , which increased the responsivity and conduction speed of the device by ensuring the charge generated in the active region needs to travel less than 20 μm to be stored in a p+/n+ region. A layer of silicon dioxide (SiO_2) was deposited over the contact regions and channels were etched to prepare the diodes for contact deposition. Figure 9 shows the diagram of the layers in the fabrication process.

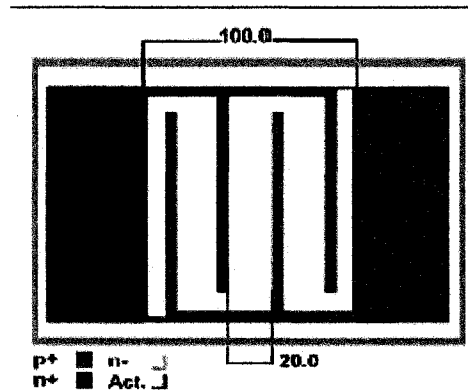


Figure 8 The interdigitated design of the p+/n+ devices.

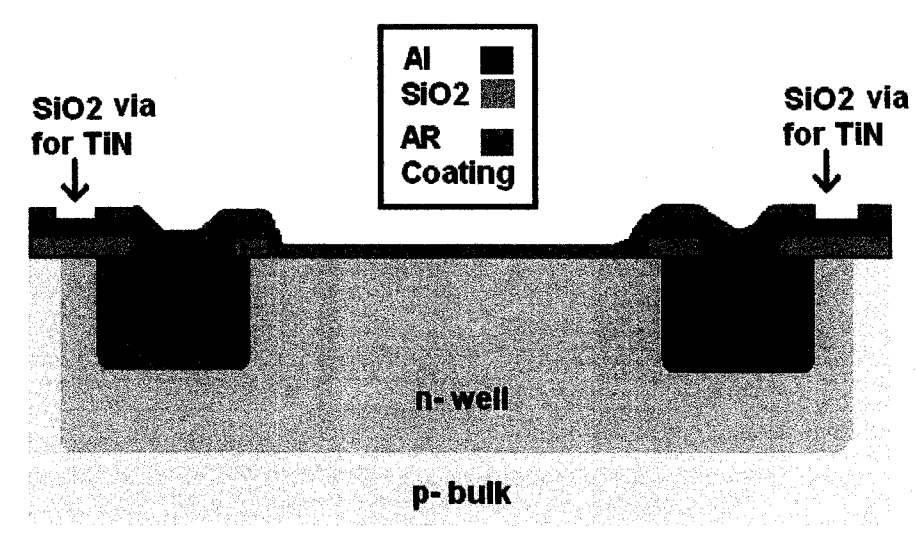


Figure 9 Cross section of the fabrication layers of the photodiode device.

Three silicon wafers were produced during the fabrication process. Each wafer contained nine sections with 142 micro-photodiodes with a chip size of 300 by 500 μm . One section of the wafer has seven sets of 22 different geometries of micro-photodiodes. The devices vary by size of Active Area (AA), Contact Area (CA), and separation distance of contacts. Table 1 lists the different photodiode types that were produced.

Table 1 List of the 22 Types of Micro-photodiodes by Device Geometry.

Diode Type	Active Area (LxW, μm)	Contact Area (LxW, μm)	Separation of Contacts (μm)	Leakage Resistor ($\text{k}\Omega$)
1	100x40	30x40	120	n/a
2	100x40	30x40	320	n/a
3	100x40	80x70	120	n/a
4	100x40	80x70	280	n/a
5	100x40	30x40	120	200
6	100x40	30x40	320	200
7	100x40	80x70	120	200
8	100x40	80x70	280	200
9	100x100	30X100	120	n/a
10	100x100	30X100	320	n/a
11	100x100	60x200	120	n/a
12	100x100	60x200	320	n/a
13	100x100	30X100	120	80
14	100x100	30X100	320	80
15	100x100	120x100	120	80
16	100x100	60x200	320	80
17	200x200	60x200	220	n/a
18	200x200	60x200	330	n/a
19	200x200	115x250	220	n/a
20	200x200	60x200	220	20
21	200x200	60x200	330	20
22	200x200	115x250	220	20

Some of the devices contain a leakage resistor, shown in Figure 10, in parallel with the contacts to discharge contact capacitance formed by the double charge layer at the electrode-electrolyte interface.

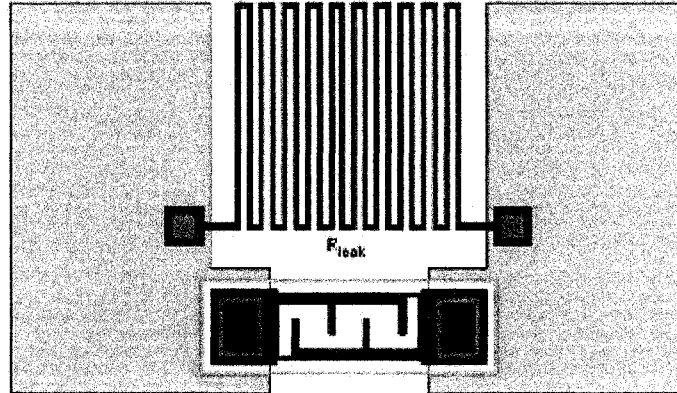


Figure 10 The layout of the leakage resistor in the micro-photodiodes.

To create the leakage resistor, a p⁺ strip was implanted into the bulk substrate parallel to the photodiode. The leakage resistance was fixed to approximately 200 K Ω by regulating the size of the strip and the concentration of the dopants. The chosen resistance limits the shunting of the current during the on cycles to 10 % and discharges the capacitance of the interface during off cycles.

3.2 Deposition of Contact Material

Two of the device wafers had TiN deposited on the contacts at the Institute for Micromanufacturing (IFM) at Louisiana Tech University. A DC-RF magnetron sputter deposition system was used to deposit a layer of TiN on two of the wafers. The TiN layer was formed using reactive sputtering in a 50% argon/ 50% nitrogen (N₂) atmosphere with a feed pressure of 2×10^{-3} Torr, an open pressure of 2×10^{-3} Torr, a throttled pressure of 5×10^{-3} Torr, and a deposition rate of 200 Å/m. One wafer was sputtered for 10 hours to a TiN thickness of 635 nm, and the second was sputtered for 14 hours to a TiN thickness of 900 nm.

The third wafer had a 350 nm layer of IrOx sputter deposited onto the contacts at Boston University. After the deposition of the three wafers, they were placed into an acetone bath to remove the resist and excess deposition from the wafers. The bath and wafer were immersed in an ultrasonic cleaner and pulsed at 40 kHz for three periods of five minutes. In between each session, the wafer was rinsed with deionized water. After the resist was removed, the wafers were diced into individual photodiodes by MicroPrecision Engineering (MPE) Inc.

After the dicing process, a small number of the IrOx coated photodiodes were selected from the third wafer to have a small layer of platinum black deposited on the contacts. Each diode was placed into a platinization solution composed of 1% chloroplatinic acid, 0.0025% HCl, 0.01% lead acetate, and deionized water. A DC current with a density of 500 mA/cm^2 was delivered into the diode for three minutes through a microelectrode touching the cathodic contact vs. a large Pt reference electrode in the solution. A white light was allowed to shine on the micro-photodiode while the current was delivered. Both the anode and the cathode were coated with platinum black at the end of this process.

3.3 Volume Conductor Measurement

The voltage generated by the coated microphotodiodes was measured in a volume conductor. The volume conductor consisted of saline diluted five times with distilled water to the specific resistivity ($300 \Omega\text{cm}$) of CNS gray matter [50]. Figure 11 shows a diagram of the volume conductor measurements. The diode to be measured was attached to the bottom of a 10 mm diameter Petri dish using modeling clay. The diluted saline was

then poured 2 mm deep into the Petri dish. A 50 mW laser (DLS-500-830FS-50, SotckerYale, Canada) was positioned over the microelectrode. A square wave pulse was used to control the laser, with 0 V turning the laser on and 5 V turning it off.

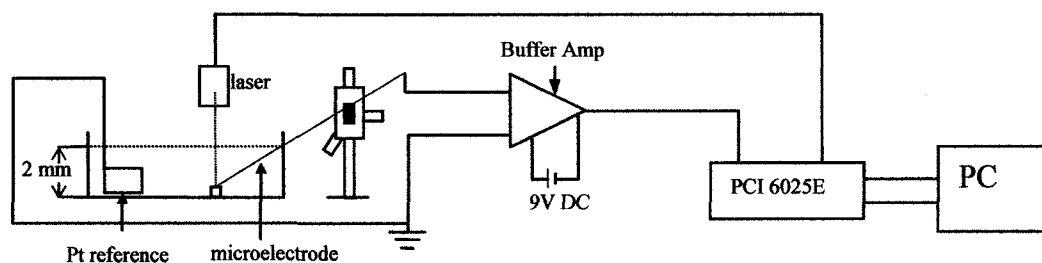


Figure 11 Diagram of volume conductor measurements.

The voltage generated in the volume conductor was measured with 76 mm tungsten microelectrodes in reference to a large Pt electrode. The positioning of the microelectrode was controlled using a WPI M325 precision micromanipulator which has 10 μm steps and error of $\pm 2\mu\text{m}$ in the x, y, and z directions. The microelectrode had a 500 μm shank diameter and a taper angle of eight degrees. The AC impedance of the electrodes was 12 $\text{M}\Omega$ at 1 KHz. A buffer amplifier stage, with a 9 V supply, was added immediately following the microelectrode to compensate for the high impedance of the electrode. Both input and output were controlled by a custom LabVIEW program.

During measurements, the microelectrode was positioned on the surface in the center of the cathode contact of the diode. The LabVIEW program is used to send a 5 ms square wave pulse at 4 Hz to the laser for 30 seconds while simultaneously recording the voltage generated in the volume. The 120 waveforms were then averaged using a Matlab program to improve the signal to noise ratio of the waveforms. The measurements were repeated in the volume conductor at 10, 20, and 30 μm above the surface of the cathode. Then, the entire series of measurements was repeated for the anodic contact.

3.4 Determination of Laser Power

A NIR laser (Lasiris, DLS-500-830FS-50, StockerYale) with a wavelength of 830 nm was used in the *in vitro* and *in vivo* experiments discussed in this work. This laser takes an input signal that adjusts the intensity of the light output. Measurements were performed to characterize the relationship between the controlling signal voltage and the light intensity. The laser power curve was experimentally determined by measuring the output light intensity of the laser with a commercially available photodiode (Optek OPF480). The photodiode has an active area diameter of 0.25 mm, a peak response wavelength of 860 nm, and a typical flux responsivity of 0.55 A/W. A custom LabVIEW (National Instruments) program modulated the laser with a square pulse (pulse width of 10 ms) ranging from 0 V (full power) to 5 V (off), in 5 mV increments. With the laser focused to 113 mm, the voltage generated by the photodiode current across a resistance of $R = 3.8 \Omega$ was measured as shown in Figure 12. The laser control LabVIEW program averaged the peak voltage generated by each pulse of a 100 pulse train and recorded this average in response to the input voltage.

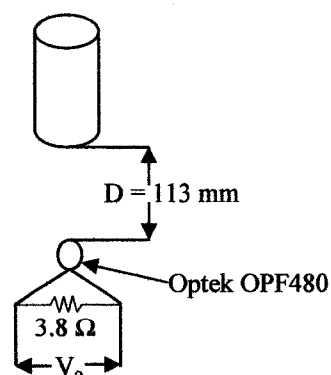


Figure 12 Diagram of laser power measurement setup.

The current I generated by the photodiode was calculated from the voltage V_o across the resistor R using Ohm's Law as shown in Equation 3.1,

$$I = \frac{V_o}{R}. \quad \text{Equation 3.1}$$

The power P of the laser was then calculated via Equation 3.2 using the active area radius and the flux responsivity F_r ,

$$P = \frac{I}{F_r r^2 \pi}. \quad \text{Equation 3.2}$$

A third order polynomial power curve was fitted to the data using the least squares method of regression analysis.

3.5 In Vivo Laser Power Threshold

3.5.1 Construction of Implant Device

A device, shown in Figure 13, was constructed to determine the implantation depth of the microstimulator during the *in vivo* experiments. The selected microstimulator was secured to a 4.0 mm x 8.0 mm x 1.0 mm piece of plastic shim stock (Precision Brand) using a two component silicon elastomer mixture (Med-4211, Silicone Technology/Nusil Technology). Two 4.0 mm x 1.0 mm x 0.5 mm pieces of plastic shim stock were glued with a 1 mm gap using instant superglue to a second 4.0 mm x 6.0 mm x 1.0 mm piece of plastic shim stock. The total thickness of the two 0.5 mm shim stock pieces was then measured using an electronic digital caliper (CEN-TECH) with a resolution of 0.01 mm. After data were collected at each depth, a 4.0 mm x 1.0 mm x 1.0 mm was glued to each of the 0.5 mm shim stock spacers for four depths of 0.5 mm, 1.5 mm, 2.5 mm, and 3.5 mm. The spacer thickness was checked using the digital calipers

after each new spacer was added. A new holding device was constructed for each experiment and microstimulator tested.

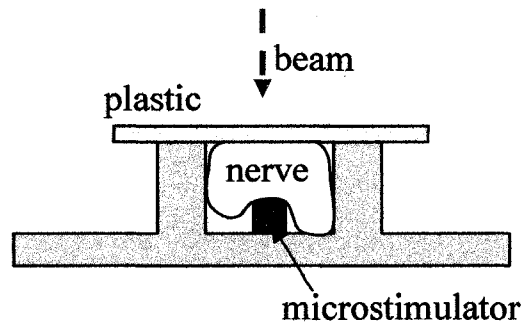


Figure 13 Device used to determine the implantation depth.

To determine the light loss caused by the 1.0 mm thick plastic, the light transmission through four pieces of plastic was tested. The block diagram of the system used to measure light transmission, a broadband (380 – 1700 nm) tungsten light source (FO-6000, World Precision Instruments), miniature fiber optic spectrometer (SD2000, World Precision Instruments), a 50 micron optical fiber, and a 100 micron optical fiber, is shown in Figure 14.

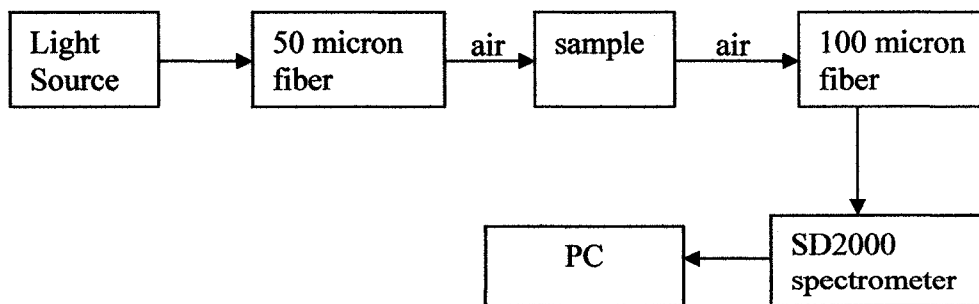


Figure 14 Block diagram of light loss experiments.

The data were collected using Ocean Optics OOIBase32 software on a Dell Inspiron 5100 with a Pentium 4 2.4 GHz processor and 768 MB of RAM. Initially, two reference spectra were collected, one with the light source on and one with the light source off, with no sample between the fibers. Then, the plastic was inserted into the sample window, and the change in light transmission at $\lambda = 830$ nm was recorded. This measurement was repeated for a total of four samples of the plastic. The recordings were then averaged together to find the percent of light transmission through the plastic. These measurements were repeated after each experiment with the specific holding device used in the experiment, after it had been cleaned with alcohol, rinsed with distilled water and allowed to air dry.

3.5.2 Surgical Procedure

All experiments in this study were conducted in accordance with the Institutional Animal Care and Use Committee (IACUC) of Louisiana Tech University. Sprague-Dawley rats weighing 250 g -400 g were given either an initial dose of ketamine and xylazine in combination or a dose of Nembutal. Maintenance doses were given approximately 30 minutes apart, based on careful monitoring of the animal's condition. The throat and hind legs were then shaved, and the animal placed on a heated surgical table at 39 °C to maintain body temperature. A tracheotomy was performed on the animal, and respiratory support was given with a small animal respirator. CO₂ output was monitored throughout the procedure. The sciatic nerve in the left leg was exposed, removed from the animal, and placed in a saline bath in an airtight specimen jar. The wound was then stapled closed. The sciatic nerve in the right leg was exposed, and a Grass stimulator was used to find the site of the minimum stimulation threshold in μ A.

The microstimulator was then placed under the nerve, and a small incision was made on the underside of the nerve. The top piece of the holding device was placed over the microstimulator and clamped into position with a nerve thickness of 0.5 mm. The laser was centered above the implanted diode, and wire EMG electrodes were implanted into the lower leg muscles that were stimulated by the photodiode. A custom LabVIEW program was used to control the laser power and pulse width, and acquire the EMG response from the leg muscles. The threshold laser power needed to achieve stimulation for pulse widths of 10 μ s to 100 μ s was determined for a depth of 0.5 mm. The clamp was then released, the holding device expanded to a thickness of 1.5 mm, and sciatic nerve tissue from the other leg placed on top of the exposed nerve until it reached a thickness of 1.5 mm. The procedure outlined above was then repeated. This process was repeated for depths of 2.5 mm and 3.5 mm. Data were collected from six animals for two microstimulator types, 18 and 19. Animals were humanely euthanized with KCl injections while under anesthesia after the experiment.

3.5.3 Modeling of In Vivo Data

The power threshold for stimulation data were entered into SAS software for statistical analysis. The power output was analyzed with respect to pulse width, implantation depth, and microstimulator type. To analyze the effect of diode type on the data, which is a categorical variable instead of a quantitative variable, an indicator variable was introduced. Indicator variables are assigned a numerical value such as zero or one to be analyzed with the data. Diode type 18 was assigned a value of zero, and diode type 19 was assigned a value of one. The data were nonlinear, so a multilinear second-order polynomial regression fitting a generalized Equation 3.3 was fit to the data.

$$y = \beta_0 + \beta_1 x_1 + \beta_2 x_2 + \beta_3 x_3 + \beta_{11} x_1^2 + \beta_{22} x_2^2 + \beta_{33} x_3^2 + \beta_{12} x_1 x_2 + \beta_{13} x_1 x_3 + \beta_{23} x_2 x_3 + \varepsilon$$

Equation 3.3

The polynomial model was a poor fit to the data, so the model was considered a candidate for linear transformation. Because the plot of the Pulse Width (PW) versus the laser power was similar to the recognized linearizable functions in Figure 15, a logarithmic transformation was performed on those two variables. The scatter plots of the independent variables implant depth and diode type versus the laser power are linear, so no transform was performed on those two variables.

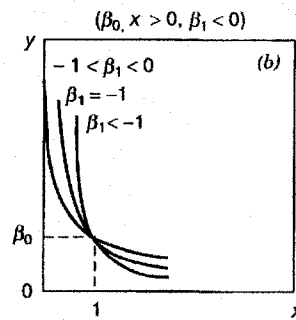


Figure 15 Linearizable functions used to select a transform [51].

A second-order polynomial regression model was performed using the two transformed variables and the two non-transformed variables. The transform of the data are shown in Equation 3.4, and the general equation of the polynomial model is shown in Equation 3.5. To check the adequacy of the model fit, an analysis of variance F test was run on the full model, and t-tests were run on the individual parameters of the model.

$$y' = \log y, \quad x'_1 = \log x_1 \quad \text{Equation 3.4}$$

$$y' = \beta_0 + \beta_1 x_1 + \beta_2 x_2 + \beta_3 x_3 + \beta_{11} x_1^2 + \beta_{22} x_2^2 + \beta_{33} x_3^2 + \beta_{12} x_1 x_2 + \beta_{13} x_1 x_3 + \beta_{23} x_2 x_3 + \varepsilon$$

Equation 3.5

3.6 In Vitro Testing of NIR Light

NIR light ($\lambda = 830$ nm) was transmitted through neural tissue to determine the minimum separation to elicit individual activation between implanted microstimulators. Because of light scattering in the tissue, the diameter of light in the tissue will spread as light travels through the tissue. The light propagation experiments studied the amount of light transmitted in a linear line from the light source to the receiver and in 0.05 mm increments from the center of the beam. This data combined with the laser thresholds from the *in vivo* experiments established the minimum distance between two implants to avoid stimulating both with one beam.

3.6.1 Experimental Setup

Figure 16 shows the overall experimental setup used to test the spatial propagation of NIR light with $\lambda = 830$ nm. A broadband (380 – 1700 nm) tungsten light source (FO-6000, World Precision Instruments) was connected to a 50 micron optical fiber and collimator and attached to a three dimensional micromanipulator. The micromanipulator was secured to a 4' x 2' optical breadboard. The light output of the collimator was set to a height of 113 mm above the receiving fiber to match laser height of the *in vivo* experiments. The spectrum data were collected with a SD2000 spectrometer (World Precision Instruments) through a 100 micron optical fiber. A Dell Inspiron 5100 with a 2.4 GHz processor and 768 MB of RAM running OOIBase32 was used to record the spectrum. The optical fiber was inserted and sealed into a small Petri dish, as shown in Figure 17. Because the tip of the fiber was 2 mm above the base of the Petri dish, a 1

mm thick piece of plastic was secured around the base of the optical fiber. A second 1 mm piece of plastic was secured over the previous piece, making the plastic level with the top of the receiving fiber. This base created a level surface even with the receiving fiber for the sample to be placed on. The Petri dish was used to control the depth of the saline used in the control experiments. The Petri dish was secured 5.0 cm above the surface of the optical breadboard.

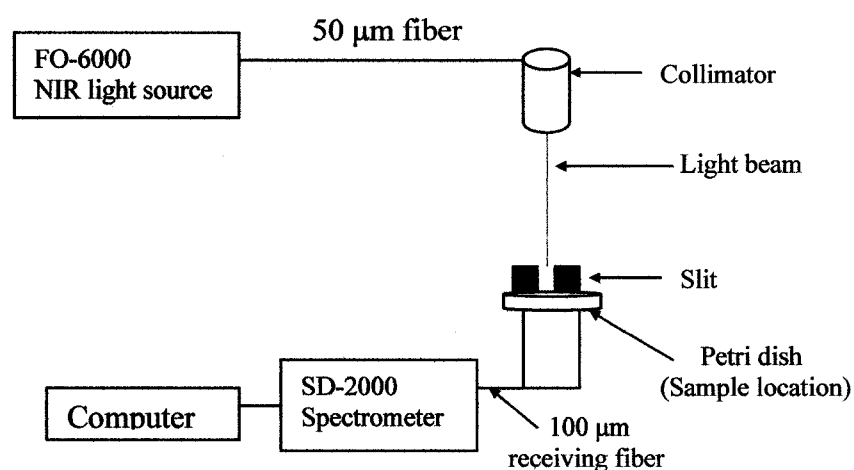


Figure 16 General setup used to measure the spatial resolution of NIR light through grey matter.

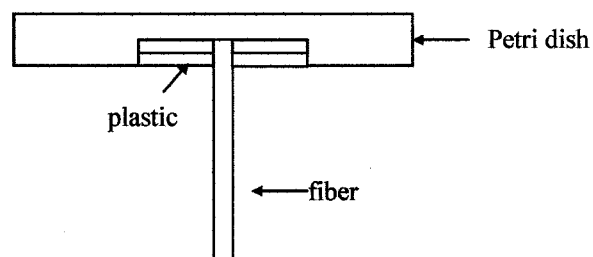


Figure 17 The setup of the 100 μm receiving fiber and tissue sample.

A 25.4 μm slit was placed between the output and receiving optical fibers to narrow the input light from 1 mm in diameter to 25.4 μm . The slit was constructed from

25.4 μm thick metal shim stock that was painted black to prevent reflection from the metal. A diagram of the slit is shown in Figure 18. The slit was centered in the light beam between the source and receiving fibers. The slit was placed 3 mm above the receiving fiber on a wooden platform held above the receiving fiber.

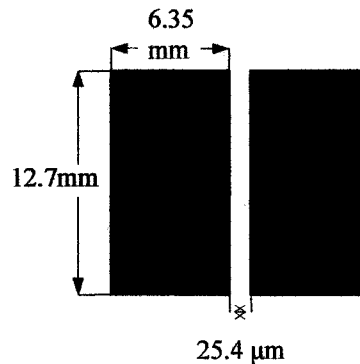


Figure 18 Slit used in light propagation experiments.

3.6.2 Construction of Holding Device

For the light propagation experiments, holding devices designed to control sample thickness were constructed following the methods outlined in section 3.4.1 of this work. Six total thicknesses were constructed and used in the data collection: 0.25 mm, 0.5 mm, 0.75mm, 1.0 mm, 1.25 mm, and 1.50 mm. The devices were used to determine the thickness of the brain tissue samples and the depth of the saline control samples. For the control samples, the Petri dish holding the receiving fiber was filled with saline to the top of the holding device. No saline came over the top of the holding device. A clamp was used to hold the device in place. For the tissue samples, the tissue was inserted into the holding device and clamped into place. Saline was then poured into the Petri dish level with the tissue sample to keep the tissue hydrated.

3.6.3 Preparation of Brain Tissue

The brain tissue from four Sprague-Dawley rats was used in these experiments. Each animal was first anesthetized with a Xylazine and Ketamine combination, and the scalp was shaved. The animal was then humanely euthanized with an injection of KCL. A Dremel saw blade was used to remove the top of the skull. After the skull was removed, the connective tissue around the brain was gently removed using a toothpick. The brain was removed from the skull cavity and placed in an airtight specimen jar, then immediately placed at 28°F controlled temperature.

To prepare the tissue for data collection, the brain tissue was removed from the freezer, and a slice of the appropriate thickness was cut from the upper layer of the left cerebral hemisphere as shown in Figure 19. The tissue sample was then allowed to thaw at room temperature (25°C) for one hour, following the method outlined by Blazek and Eggert [20]. After the thaw time, the sample was placed in the holding device and clamped into place. A saline bath was then added to the Petri dish to keep the sample hydrated. A fresh sample was used each time data were collected. Tissue sample thicknesses of 0.25 mm, 0.5 mm, 0.75 mm, 1.0 mm, 1.25 mm, and 1.50 mm were used in the data collection. Samples thicker than 1.50 mm were not used because the broadband light source was not strong enough to penetrate the thicker tissue.

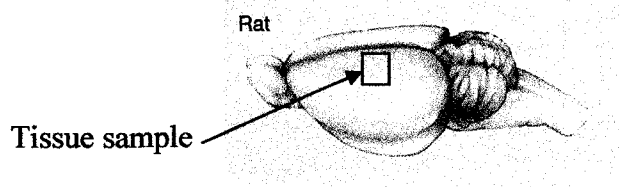


Figure 19 Location of brain tissue sample.

3.6.4 Data Collection

Once the sample was in place, the light output was centered over the receiving fiber. The FO-6000 was allowed 15 minutes of warm-up time to allow the light output to stabilize before readings were taken. The light intensity at $\lambda = 830$ nm into the receiving fiber was measured using the OOIBase32 software by Ocean Optics. Light intensity was measured on a scale of 0 to 4000 intensity counts (IC). The integration time was increased until the peak intensity was approximately 3000 IC. Integration times of 300 ms to 900 ms were used for the saline control samples. Integration times of 1.5 s to 15 s were used for the brain tissue samples. For all samples, three data sets were taken and averaged by the OOIBase32 software before recording. A dark reference was taken with the broadband light source shuttered, and then a reference was taken with the broadband light source shining into the receiving fiber. The source fiber was kept still in the z and y direction, but was moved in the $\pm x$ direction in 0.05 mm increments from the peak intensity, as shown in Figure 20. The height, z, between the receiving fiber and the sample was a constant 113 mm. The distance from the center was randomly selected until the intensity was less than 20% of the peak intensity.

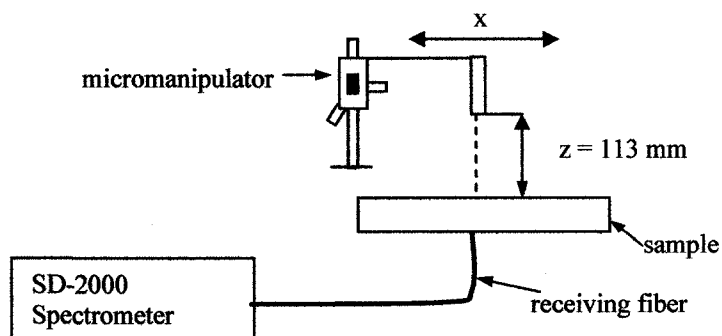


Figure 20 The movement of the light source in relation to the tissue sample and receiving fiber.

CHAPTER 4

RESULTS

4.1 Volume Conductor Response of Photodiodes

Figure 21 shows the geometry of diode types 19 and 22 of the photodiodes designed for this work. The two diode types have identical geometries, but diode type 22 includes a 20 k Ω leakage resistor. The 22 diode types consist of 11 distinct geometric pairs, one with a leakage resistor and one without. All of the diodes are 500 x 300 μm , but the size of the contacts, active areas, and separation of contacts differs. The specific geometry of each diode type can be seen in Table 1.

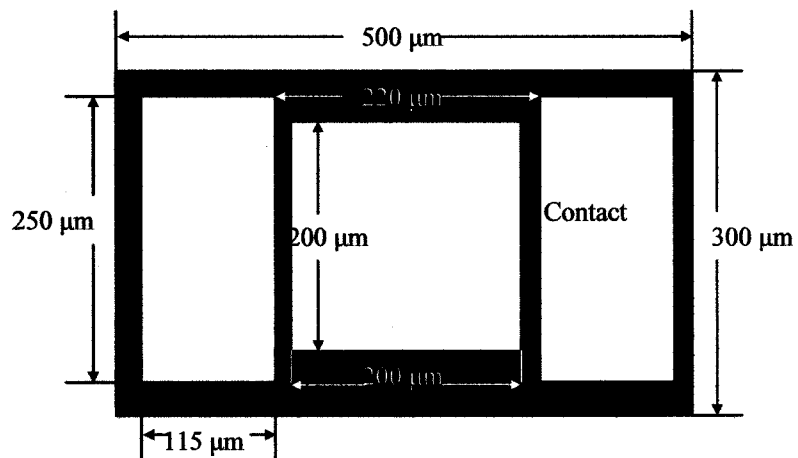


Figure 21 The geometric layout of diode types 19 and 22.

4.1.1 Iridium Oxide

The voltage generated on the surface of the sputtered IrOx cathode of diode type 22 upon illumination by the NIR source is shown in Figure 22. Diode type 22, the largest diode geometry, is shown because it generated the largest response in the volume conductor. On the surface of the contact, the diode generates -400 mV initially and slowly charges to -448 mV during the remainder of the pulse. The voltage discharges quickly when the laser is turned off. The laser power is strong enough to saturate the diode. The surface response of the Pt and TiN diodes is similar to the IrOx response. However, only a fraction of the surface voltage is transferred into the volume conductor through the electrode-electrolyte interface, where the difference in the contact materials can be readily seen. Figure 23 shows the voltage generated in the volume conductor 10 μm above the surface of the contact. The surface voltage of -448 mV quickly drops to -64 mV a short distance from the contact. The initial peak followed by a quick decay indicates a largely capacitive component to the charge transfer. The very slight elevation of the voltage above the baseline indicates an insignificant faradic component to the voltage. The diode begins to discharge only 0.05 ms after the laser is turned on and 0.15 ms before the laser is turned off. The time constant for the diode is 4 μs , which indicates a very quick discharge of the voltage, limiting the charge delivered to the conductor. The diode delivers a total charge of 0.0879 μC in a 200 μs pulse with a charge injection rate of 0.3474 mC/cm^2 .

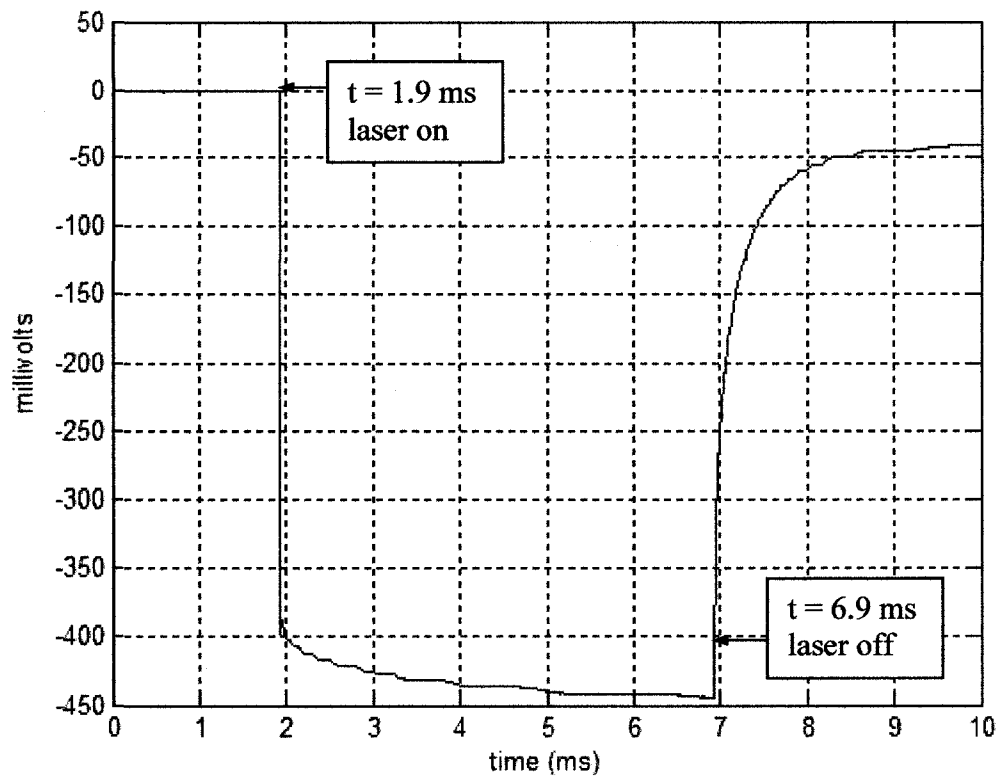


Figure 22 The voltage generated on the surface of the IrOx cathode of diode type 22 in the volume conductor.

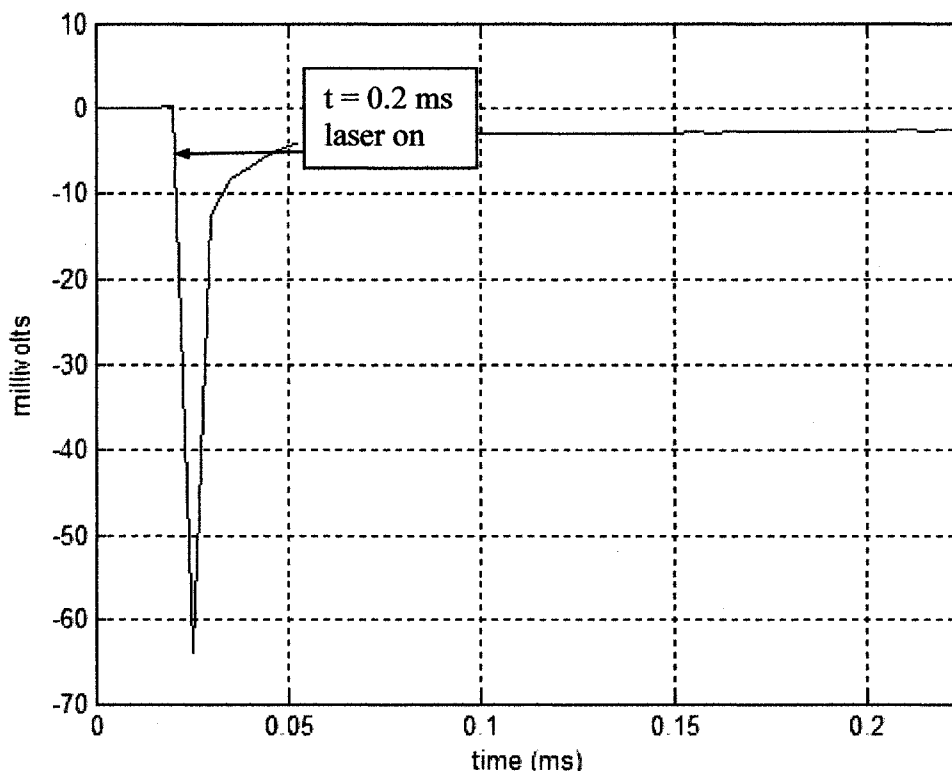


Figure 23 The voltage generated in the volume conductor just above the surface of the IrOx cathode of diode type 22 during the first 200 μs of the laser pulse.

4.1.2 Platinum

The response on the surface of the Pt contact is similar to the response for IrOx surface on the same diode. However, the amount of charge transferred across the electrode-electrolyte interface is much larger with the Pt black diode. Figure 24 shows the voltage generated in the volume conductor 10 μm above the surface of the cathode. The initial peak for the Pt diode is -210 mV, 3.2 times larger than the peak for the IrOx. The large peak followed by the slower decay, with a time constant of 41 μs , shows a predominantly capacitive charge transfer with a small faradic component. Due to the large peak and slower decay, the Pt coating is able to deliver 0.270 μC of charge during a 200 μs pulse. The charge density injected by the diode was 0.939 mC/cm^2 , well over the limits for reversible faradic transfer. After one hour of constant pulsing at 10 Hz with a

pulse width of 200 μs , the peak voltage fell to -48 mV and the injected charge density to 0.227 mC/cm^2 . Soft mechanical rubbing with a q-tip removed the Pt black coating from the contact. This indicates that the Pt black would also be easily removed on implantation into a nerve. Both the Au and TiN surface under the Pt were equally susceptible to loss of Pt due to mechanical rubbing.

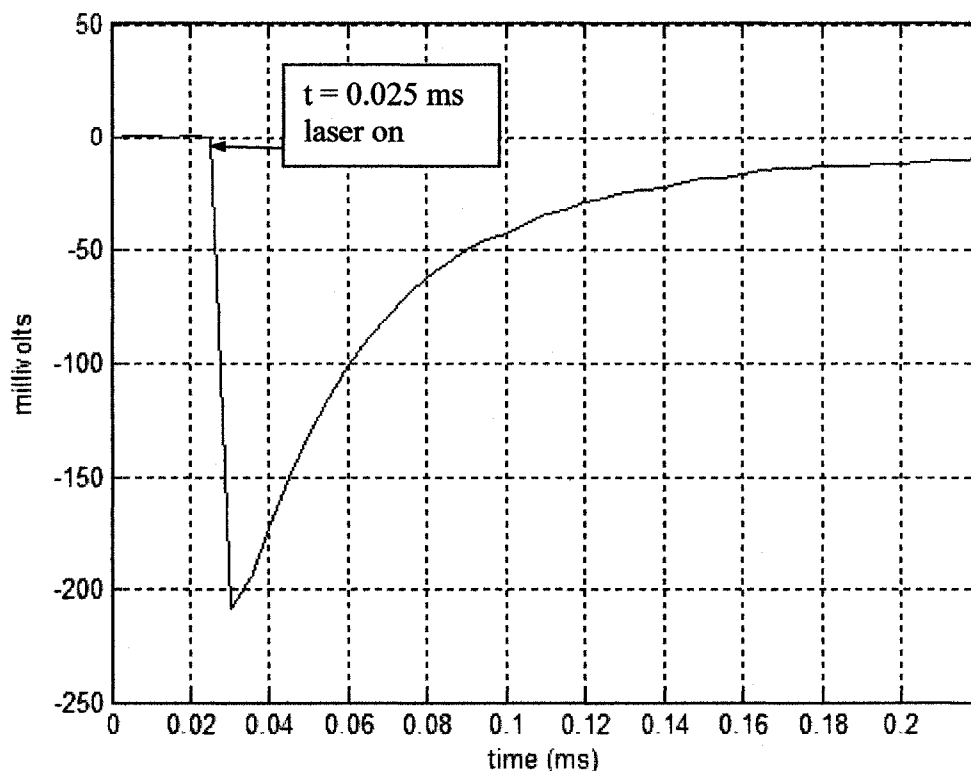


Figure 24 The voltage generated in the volume conductor just above the surface of the Pt cathode of diode type 22 during the first 200 μs of the laser pulse.

4.1.3 Titanium Nitride

The voltage generated at the surface of the TiN sputtered contact of diode type 1 is shown in Figure 25. Because the diodes are saturated, the voltage on the surface of the cathode contact is very similar for all diode types despite differences in contact area.

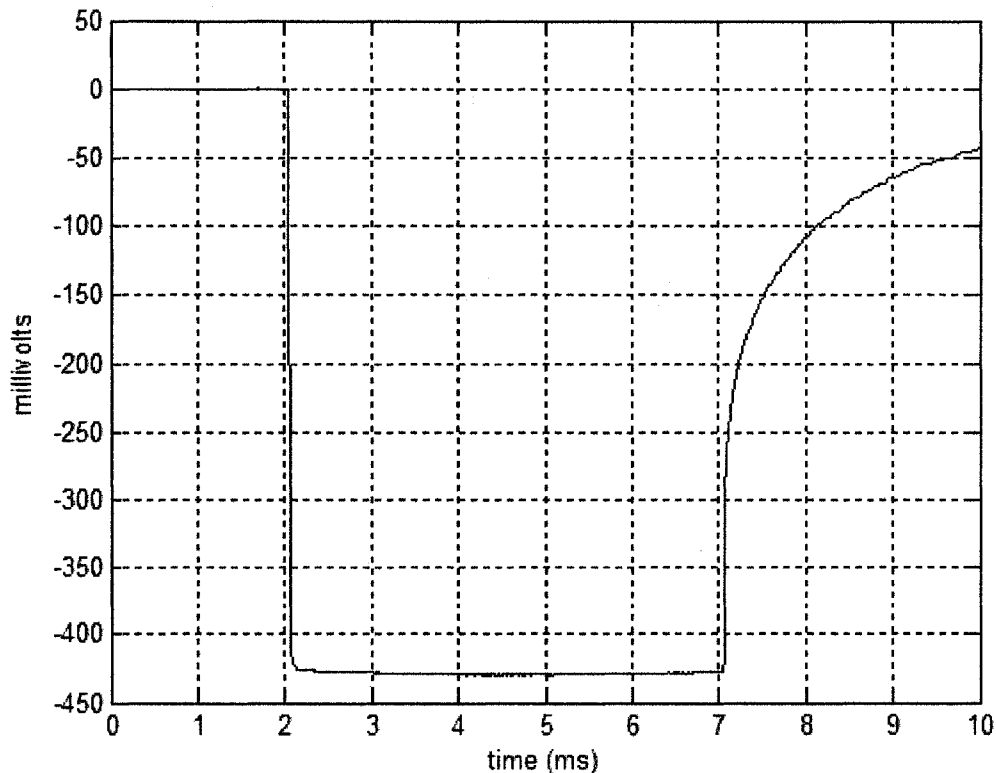


Figure 25 The voltage generated on the surface of the TiN cathode of diode type 1 in the volume conductor.

Figure 26 shows the voltage generated in the volume conductor $10\ \mu\text{m}$ above the cathode of the TiN sputtered diode type 1. Despite having a contact area of only $1200\ \mu\text{m}^2$, compared to the $28750\ \mu\text{m}^2$ contact area shown in Figure 27, the TiN sputtered diode has a large peak voltage of $-91\ \text{mV}$ and slower decay with a time constant of $70\ \mu\text{s}$. The response is mainly capacitive, but the $-10\ \text{mV}$ level below the baseline at the end of the pulse shows a small faradic component. The total charge injected into the volume during the $200\ \mu\text{s}$ pulse is $0.079\ \mu\text{C}$.

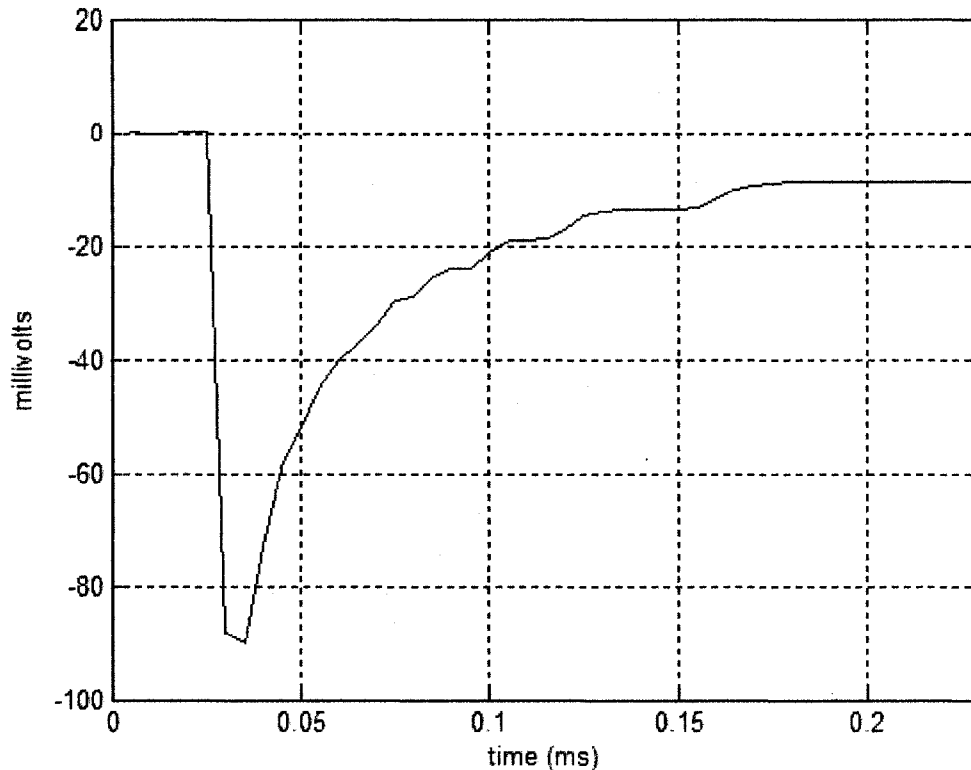


Figure 26 The voltage generated in the volume conductor just above the surface of the TiN cathode of diode type 1 during the first 200 μs of the laser pulse.

The voltage generated in the volume conductor 10 μm above the surface of the TiN sputtered contact of diode type 15 is shown in Figure 27. Diode type 15 has a contact area of 12000 μm^2 , 10 times the size of diode 1. The peak voltage of -241mV is approximately four times higher than the peak voltage of the smaller TiN sputtered diode type and displays a larger faradic component with a voltage elevated -20 mV above the baseline at the end of the pulse. The diode delivers 0.1344 μC of charge during the 200 μs pulse, a charge density of 1.12 mC/cm^2 .

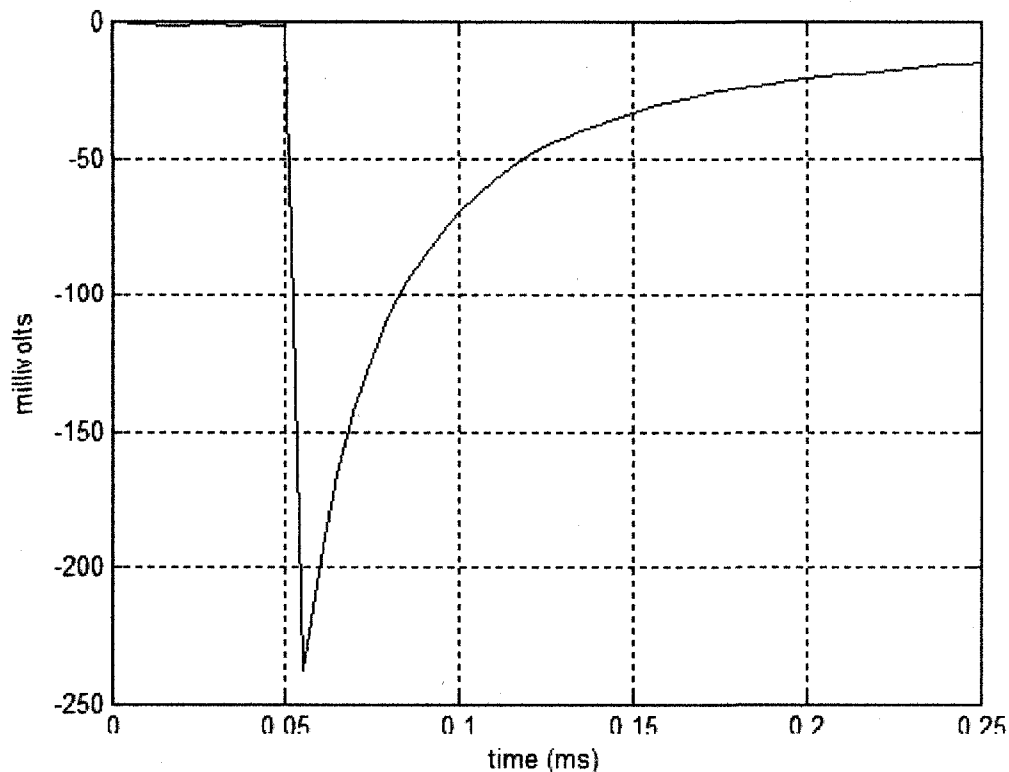


Figure 27 The voltage generated in the volume conductor just above the surface of the TiN cathode of diode type 15 during the first 200 μ s of the laser pulse.

Figure 28 shows the voltage generated 10 μ m above the TiN sputtered contact of diode type 18. Diode 18 has the same area as the diode 15 from Figure 27, but has an active area 4 times as large. The peak voltage for this diode is -93 mV, lower in absolute value than was seen on the previous TiN sputtered diodes. The decay rate is also more rapid for this diode. The total charge delivered for a 200 μ s pulse is 0.0647 μ C, a charge density of 0.54 mC/cm².

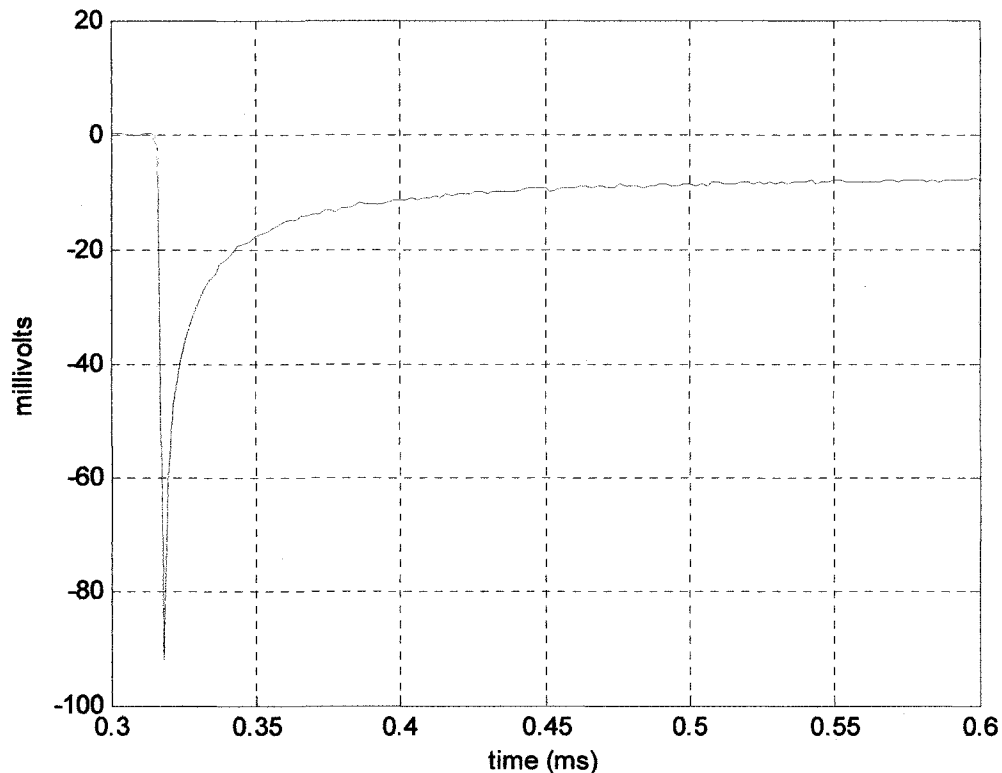


Figure 28 The voltage generated in the volume conductor just above the surface of the TiN cathode of diode type 18 during the first 200 μs of the laser pulse.

The voltage generated 10 μm above the surface of the TiN sputtered contact of diode type 19 is shown in Figure 29. Diode 19 has the same contact area and active area as diode 22, but does not have leakage resistor. This diode shows both a substantial capacitive component with the large peak of -233 mV and time constant of 216 μs and a significant faradic component with the elevated baseline of 86.4 mV at the end of the pulse. The total charge delivered by this diode was 0.4115 μC in a 200 μs pulse, a charge density of 1.43 mC/cm^2 .

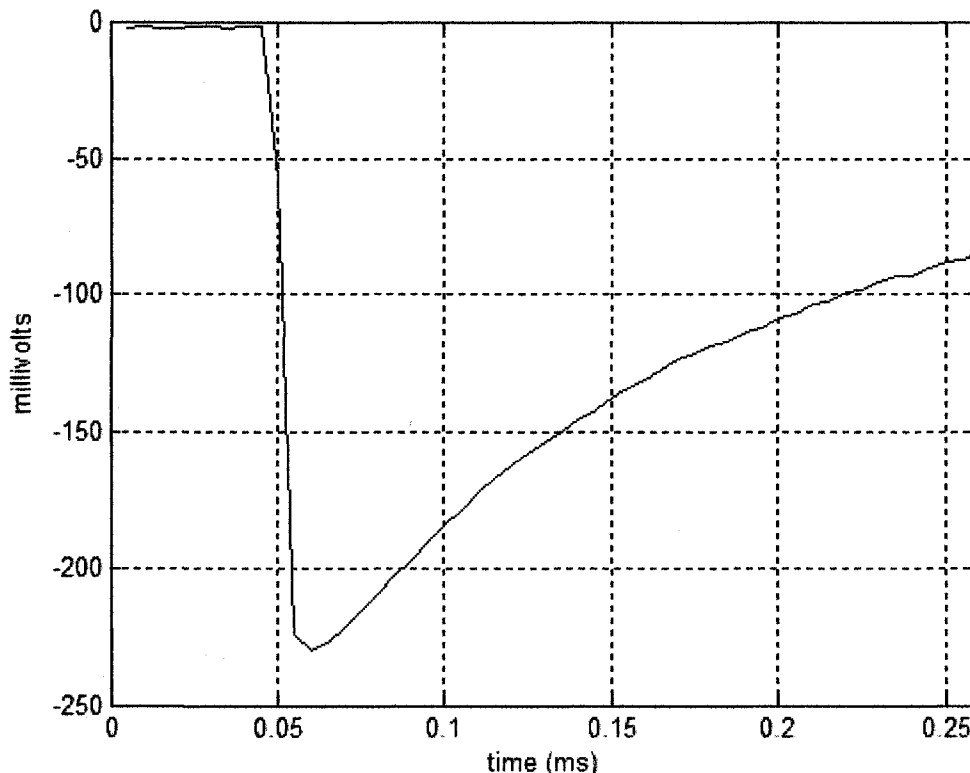


Figure 29 The voltage generated in the volume conductor just above the surface of the TiN cathode of diode type 19 during the first 200 μ s of the laser pulse.

Because diode types 15, 18, and 19 delivered the most charge in the volume conductor, these diode types were selected for *in vivo* implantation. Other large diode types did not generate the voltage expected based on the contact area and separation. The low voltage output is suspected to be due to problems with the lift-off process of the diodes. TiN charge injection is dependent on the thickness of layer, therefore a second wafer was coated with TiN at a thickness of 900 nm. The lift-off process for the thicker TiN layer was a failure and none of these diodes were tested.

4.2 EMG Response to Microphotodiodes

Figure 30 shows the single EMG response of a rat calf muscle in response to a pulse generated by a TiN coated photodiode type 19 in response to a computer generated

laser pulse. Figure 30 A shows the computer generated pulse sent to the laser, and part B shows the EMG response of the rat calf muscle a few ms later. A visual movement of the calf muscle and the rat's foot can be seen in time with the laser pulsing. Figure 30 proves that a microphotodiode can generate enough charge to produce a response in the rat PNS.

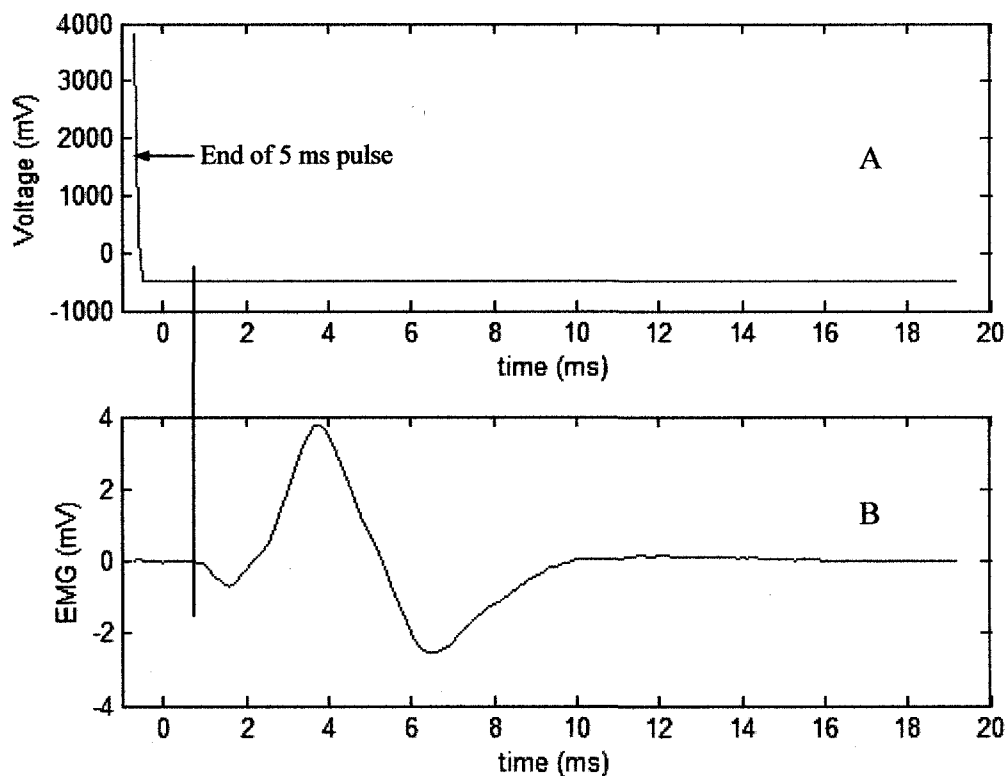


Figure 30 The EMG response of the calf muscle of a rat in response to a single pulse laser stimulation of a photodiode implanted into the sciatic nerve.

Figure 31 shows the EMG response of the photodiode being pulsed for 5 ms intervals with a frequency of 10 Hz. The square wave control signal to the laser is shown in Part A, and the EMG response following each pulse. The rat's foot moved up and down at a frequency of 10 Hz in response to the laser. The photodiode is capable of charging and discharging fast enough to keep up with the 10 Hz frequency.

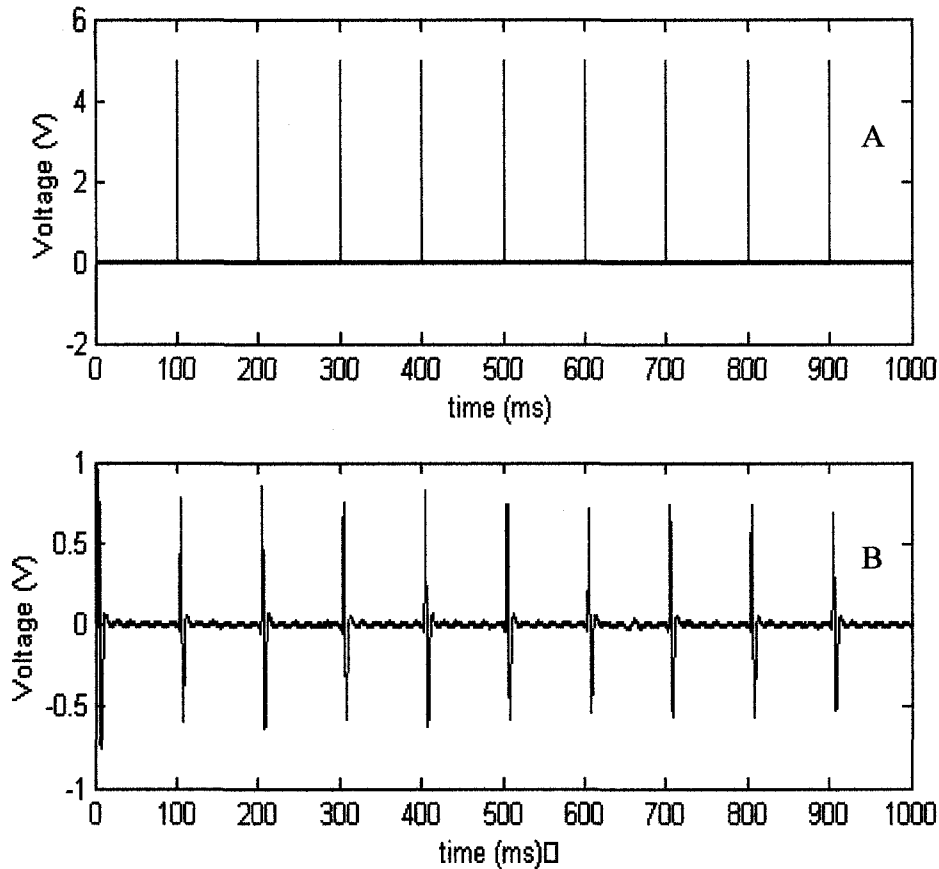


Figure 31 The EMG response of the calf muscle of a rat in response to laser stimulation of a photodiode implanted into the sciatic nerve, repeated with a frequency of 10 Hz.

Figure 32 shows the EMG response of the rat calf muscle in response to the laser pulsing at 50 Hz. At this frequency, a strong EMG response is observed for the first two pulses and then tetanus of the muscle occurs. Visually, a steady contraction of the calf muscle is observed with the foot held in a raised position. The tetanus and lack of EMG is not due to the diode but because of the sustained contraction of the muscle fibers at this frequency.

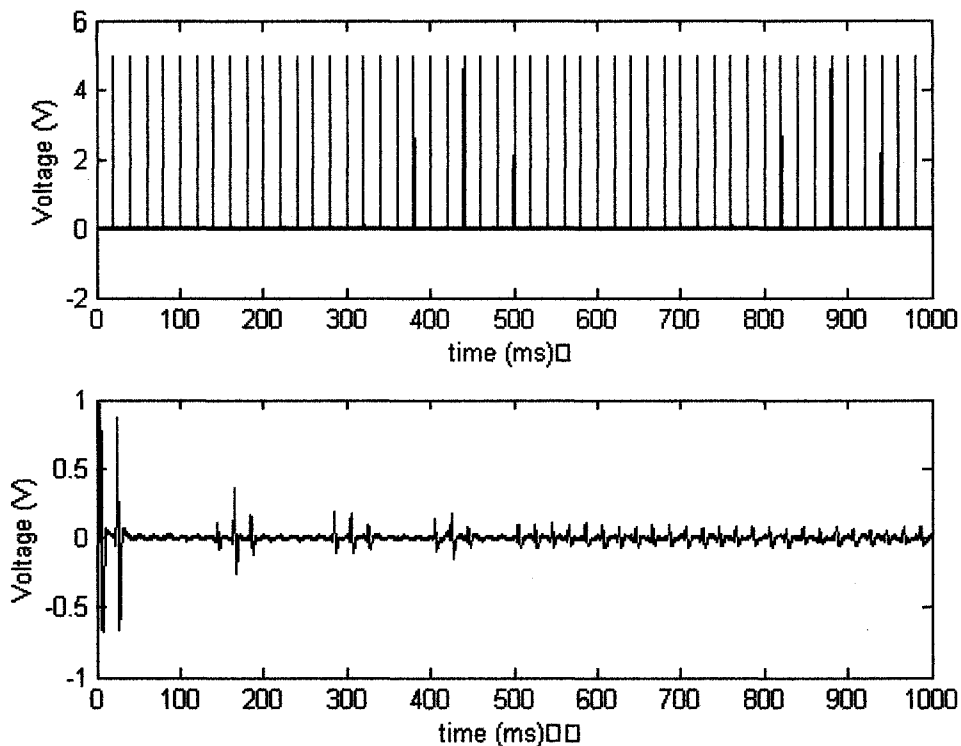


Figure 32 The EMG response of the calf muscle of a rat in response to laser stimulation of a photodiode implanted into the sciatic nerve, repeated with a frequency of 50 Hz.

4.3 Laser Power Curves

The power output curve of the Lasiris laser ($\lambda = 830 \text{ nm}$) in response to a square wave input was determined by measuring the voltage output of a Optek OPF480 photodiode in response to the laser. The power generated by the laser was calculated from the voltage response, shown in Figure 33, across a 3.8Ω resistor using Equations 3.1 and 3.2. Figure 34 shows the resulting power curve and the third order polynomial fit to the data. The fitted data has an R^2 value of 0.9995, indicating a good fit of the data. The fitted equation is shown in Equation 4.1. The laser specifications indicate that a 0 V input is full power and a 5 V input is off. The experimental data shows full power output is level with input voltages of 0 V to 0.5 V, then power level slowly falls. When the input voltage is increased to 4 V and above, the power output is approximately zero.

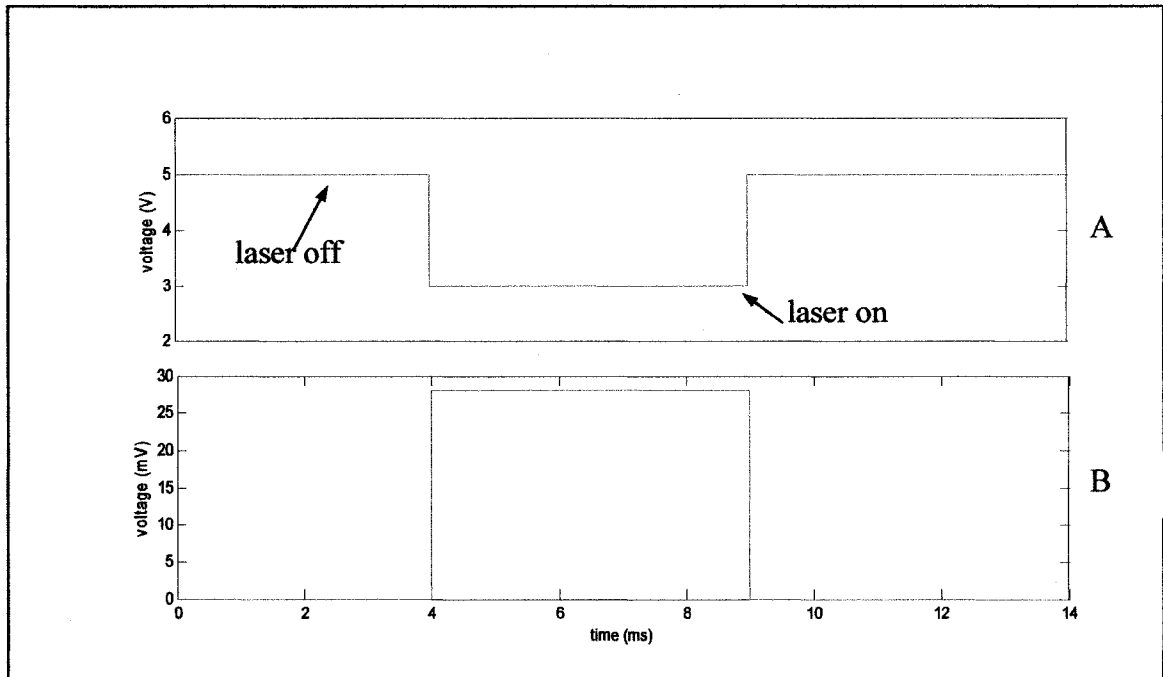


Figure 33 Part A shows the square wave input to the laser. Part B show the voltage generated across a 3.8 Ω resistor by the Optek OPF480.

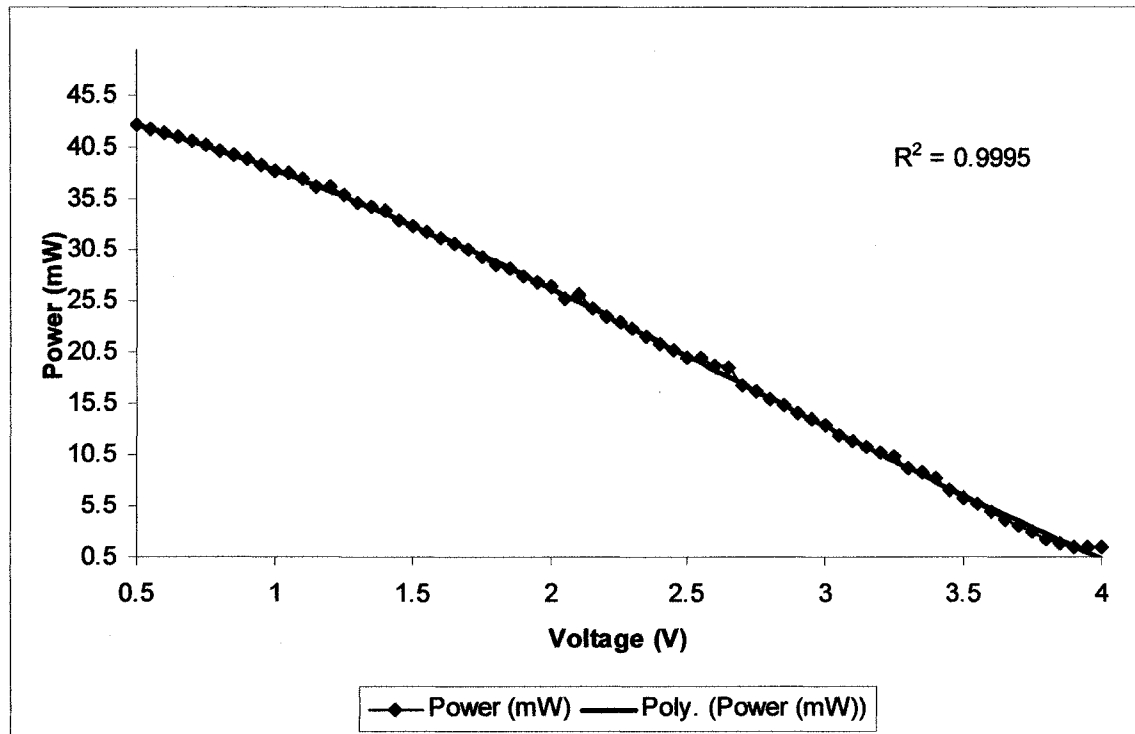


Figure 34 Power curve fit of the Lasiris laser.

$$y = 45.527 - 4.0791x - 3.4886x^2 + 0.4208x^3. \quad \text{Equation 4.1}$$

4.4 In Vivo Laser Power Threshold

Figure 35 shows the minimum-power threshold for each pulse width required to stimulate the sciatic nerve with diode type 18, with four different thicknesses of the neural tissue. Figure 36 shows the same information for diode type 19. For all implantation depths, the power needed to cause stimulation remains stable across longer pulse widths but then experiences a sharp increase once the pulse width decreases beyond a certain point. The power threshold at all pulse widths increases as implantation depth increases for both diode types. The stability of the power threshold for longer pulse widths implies that the energy needed for stimulation is delivered in the early portion of the pulse, and the longer pulse widths are not needed.

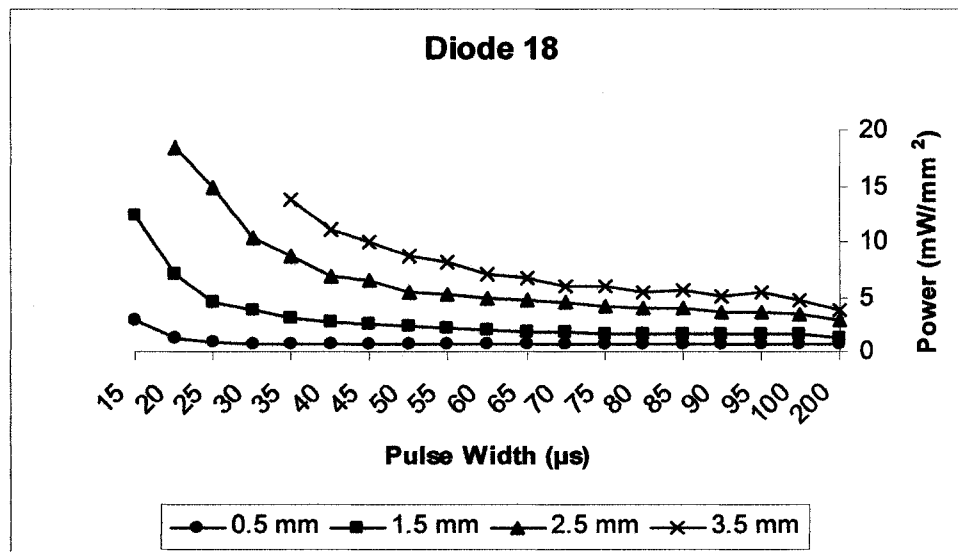


Figure 35 Laser power stimulation thresholds for diode type 18 for four thicknesses of neural tissue.

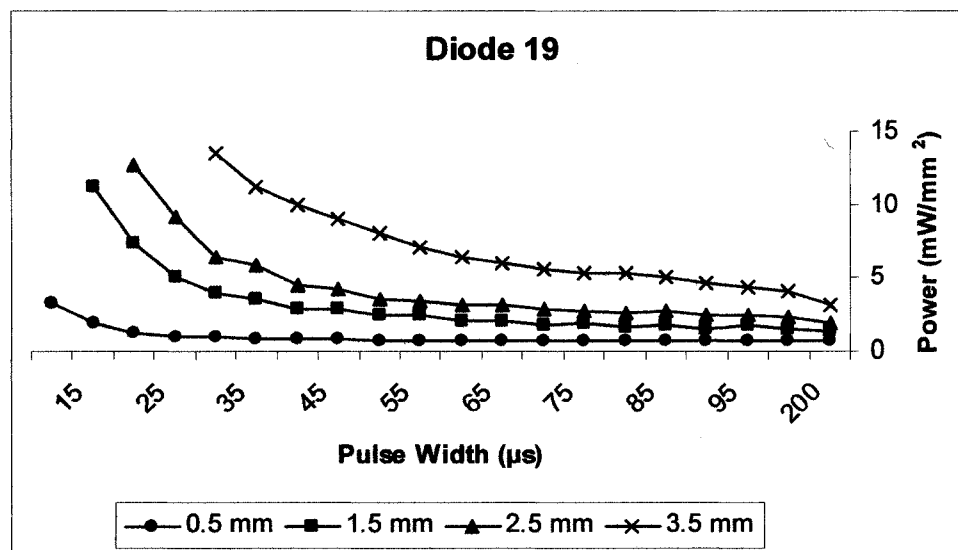


Figure 36 Laser power stimulation thresholds for diode type 19 for four thicknesses of neural tissue.

Table 2 shows the analysis of variance of a curve fit for the stimulation threshold data for both diode types. Table 3 shows the testing of the parameter estimates for the model. The adjusted R^2 value for the model is 97.9%, implying that the model can

explain 97.9% of the variability in the data. The predicted R^2 value of 97.7% indicates that the model will accurately predict new data. The t tests for the parameter estimates show that all six parameters have p values less than 0.0001, indicating that they are all important to the model fit. This statistical test allows us to accept the hypothesis that the diode type has a significant effect on the stimulation threshold at a certain pulse width.

Table 2 ANOVA for the Stimulation Threshold Data Fit.

Analysis of Variance					
Source	Degrees of Freedom	Sum of Squares	Mean Square	F value	Pr > F
Regression	6	22.21	3.70	1088.31	0.000
Residual Error	137	0.47	0.0034		
Total	143	22.67			

$$R^2 \text{ (adjusted)} = 97.9\% \quad R^2 \text{ (predicted)} = 97.7\%$$

Table 3 Parameter Testing for the Stimulation Threshold Data Fit.

Predictor	Parameter Estimate	Standard Error	t value	Pr > [t]
Constant	2.45	0.152	16.12	0.00001
log (PW)	-3.02	0.181	-16.71	0.00001
Depth	0.973	0.039	25.16	0.00001
log (PW) ²	0.786	0.055	14.33	0.00001
DepthxDiode	0.031	0.0044	7.02	0.00001
Depth ²	-0.064	0.005	-12.82	0.00001
log (PW)xDepth	-0.244	0.0201	-12.13	0.00001

Equation 4.2 shows the fitted equation for the model. Indicator variable x_3 was used to quantify diode type, using a zero for diode type 18 and a one for diode type 19. The use of the indicator variable creates two equations: without the interaction term between implant depth and diode type for diode 18 and with the interaction term for diode 19. Figure 37 compares the minimum power predicted by Equation 4.2 for diode

type 19 at an implant depth of 0.5 mm to the experimental data. Although a good predictor of the power threshold for stimulation, the model overestimates the power needed for $PW < 35 \mu s$.

$$\log y = 2.45 - 3.02 \log x_1 + 0.974x_2 + 0.786(\log x_1)^2 + 0.031x_2x_3 - 0.064x_2^2 - 0.244(\log x_1)x_2,$$

Equation 4.2

where

y = laser power,

x_1 = PW,

x_2 = implant depth, and

x_3 = diode type.

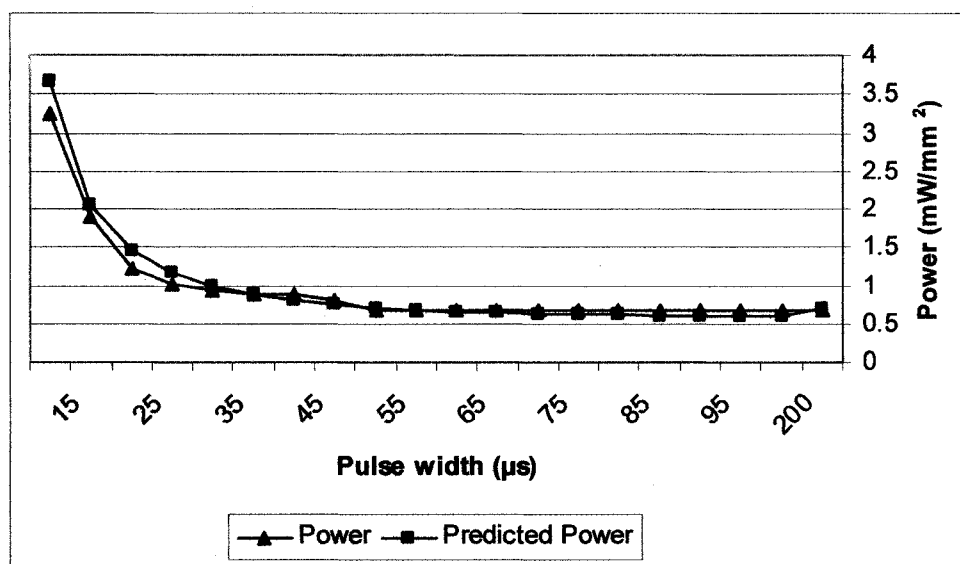


Figure 37 The power needed for stimulation for diode 19 at 0.5 mm vs. the power predicted by the model.

Figure 38 compares the minimum pulse width for stimulation at each implantation depth between the two diode types. Diode 18, which has a smaller contact area than diode

19, requires a longer pulse width for stimulation than diode 19 at the minimum and maximum implantation depths. Because the difference in pulse width is only 5 μs and because the same difference is not observed for all pulse widths, these data do not imply a significant difference in the diode geometries.

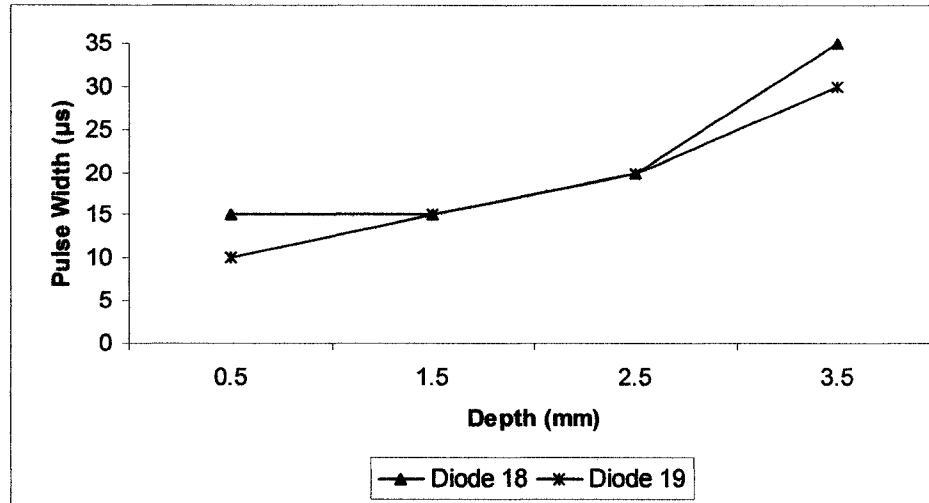


Figure 38 Minimum pulse width for stimulation at each depth.

Figure 39 shows the optimum pulse width for stimulation at each implantation depth for both diode geometries. The optimum pulse width was defined as the pulse width with minimum energy and power thresholds. It's value determined by plotting the power threshold vs. the energy threshold at each pulse width. The optimum pulse width increases as implantation depth increases for both diode geometries. The similarity of the plots for both diodes implies that there is little difference between the two geometries.

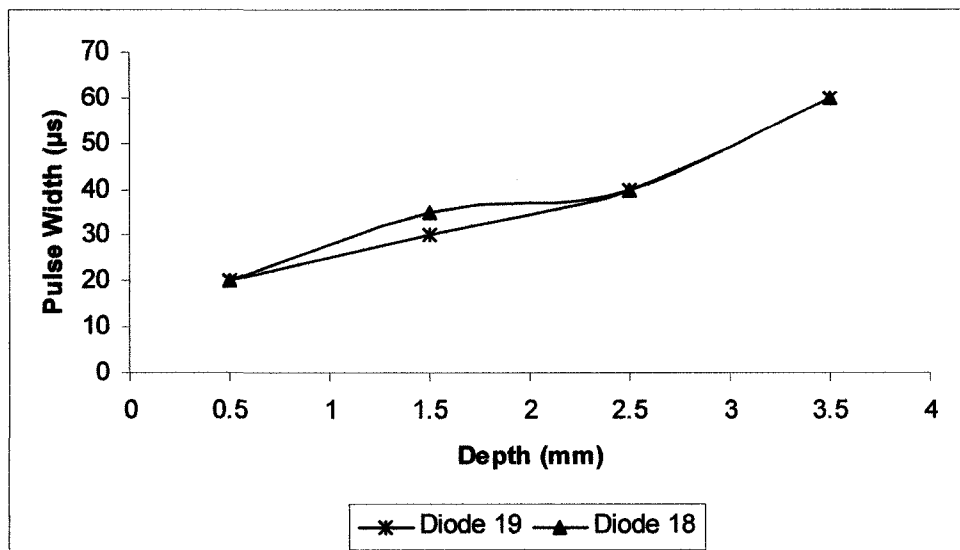


Figure 39 Optimum pulse width for stimulation at each depth.

Figure 40 compares the power-stimulation threshold for each diode geometry at a pulse width of 200 µs. The threshold is the same for the first two depths, but diode 18 requires more power than diode 19 at the two deeper implantations. This is evidence that diode 18 requires more power to transfer the same amount of energy into the tissue as diode 19. This result is expected because of the smaller contact size of diode 18 as compared to diode 19.

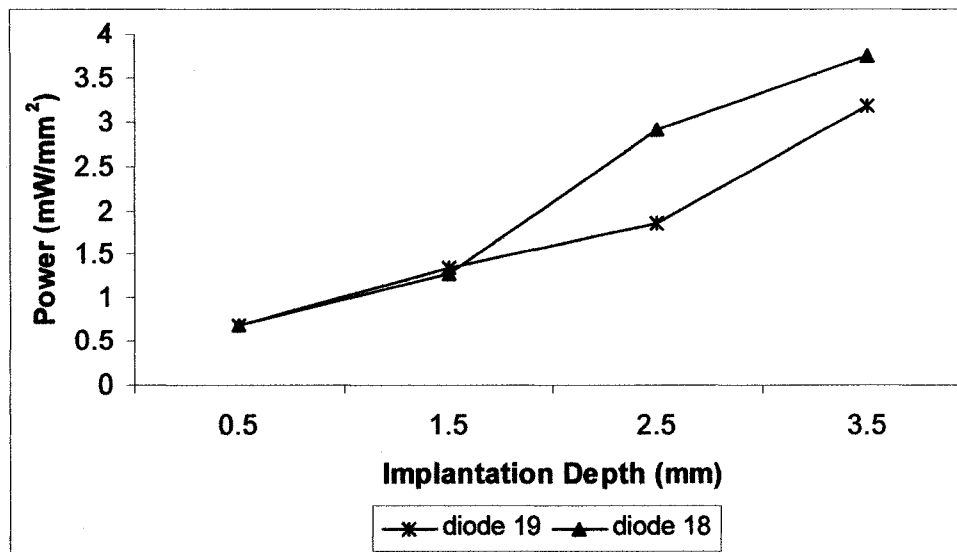


Figure 40 Power threshold at PW = 200 μ s.

4.5 NIR Light Propagation

Figure 41 shows the propagation of NIR light through six depths of saline as the source light is moved in 0.5 mm increments horizontally from the receiving light fiber. Figure 42 shows the propagation of NIR light through six depths of brain tissue as the source light is moved in 0.5 mm increments horizontally from the receiving light fiber. The amount of light transmitted through the sample as the light is moved away from the receiving fiber is much higher for the tissue sample than the saline sample, indicating an increase in light scattering. The propagation through the tissue changes more as depth increases than the propagation through saline. The transmission profile through the brain tissue is much less symmetric than that of the saline. This is not surprising as saline is homogeneous, but the heterogeneous structure of brain tissue results in changing optical properties for different areas of the brain.

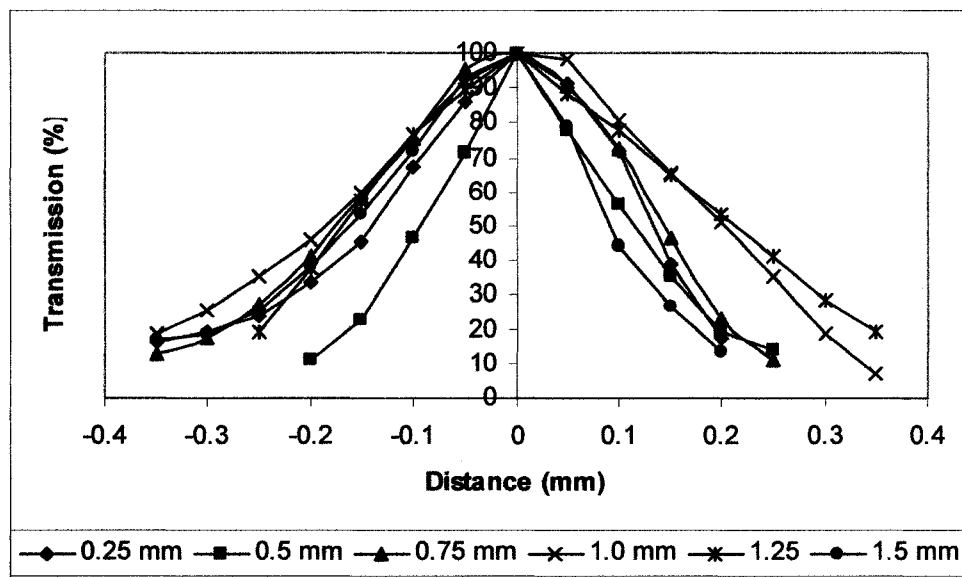


Figure 41 NIR light propagation horizontally through the saline.

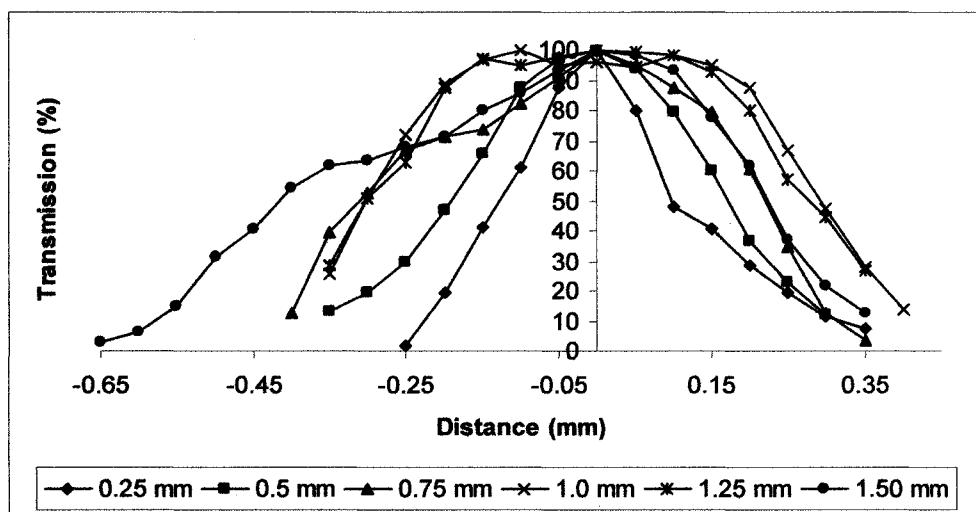


Figure 42 NIR light propagation horizontally through the brain tissue.

Figures 43 and 44 show the light signal at depths of 0.5 mm and 1.25 mm, respectively, as a function of the source position for both saline and tissue. These figures confirm the increased scattering of the light through the tissue as compared to the saline at a sample thickness of 0.5 and 1.25 mm. At a depth of 0.5 mm, 70% of the light is transmitted through the saline at a diameter of 0.1 mm from the source fiber and through

the tissue at a diameter of 0.27 mm from the source fiber. For the sample thickness of 1.25 mm, 70% of the light is transmitted through the saline at a diameter of 0.2 mm from the source fiber and through the tissue at a diameter of 0.48 mm from the source fiber.

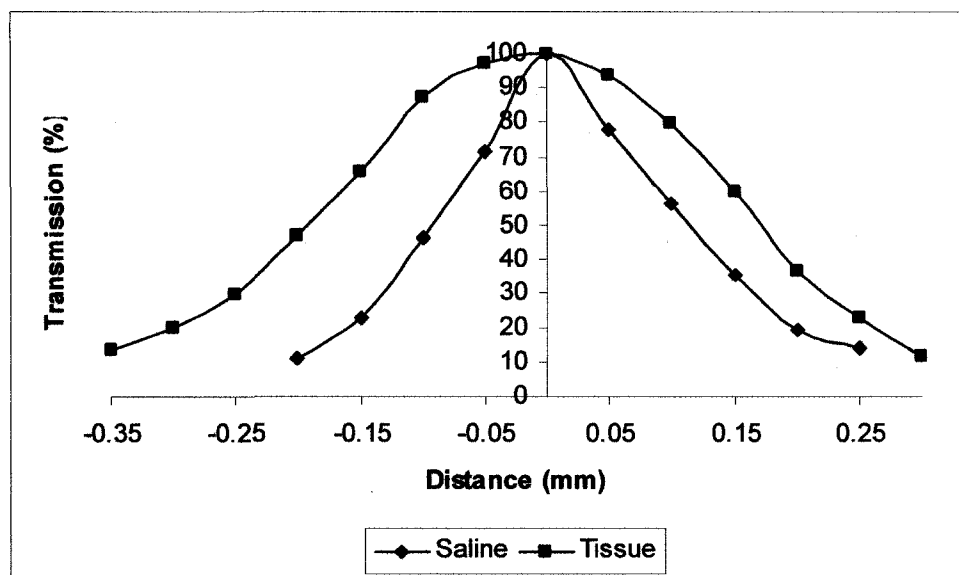


Figure 43 NIR light propagation at 0.5 mm thickness.

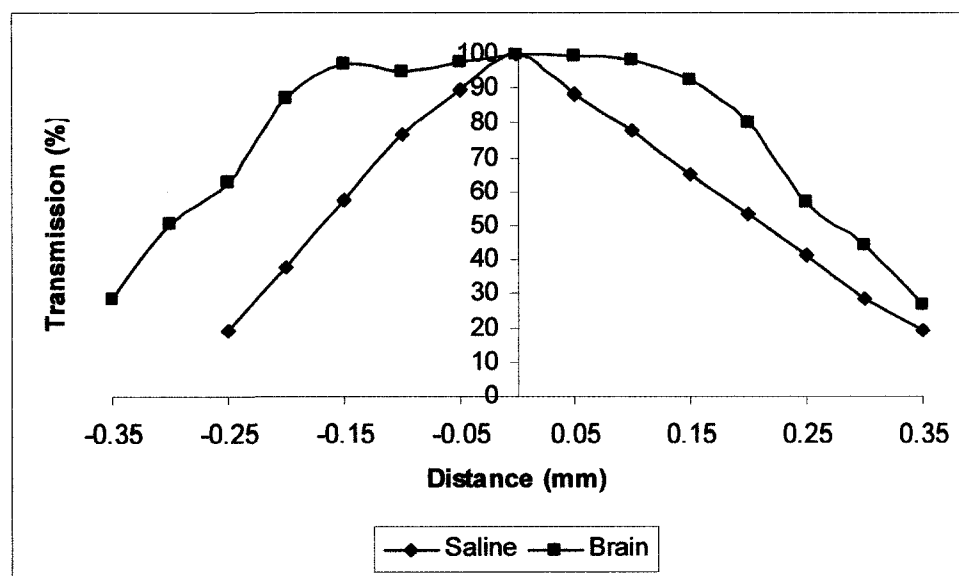


Figure 44 NIR light propagation at 1.25 mm thickness.

Table 4 shows the analysis of variance for a second order polynomial model of the three experimental parameters: sample thickness, distance from center, and sample type. Table 5 shows the testing of the significant terms in the model: the horizontal distance from the receiving fiber, the square of the sample type, the interaction of the distance and the sample thickness, and the interaction of the sample thickness and type. The model indicates a significant difference on the effect of light transmission of saline versus brain tissue.

Table 4 ANOVA of 2nd-order Model Valid for $d < 0$.

Analysis of Variance					
Source	Degrees of Freedom	Sum of Squares	Mean Square	F value	Pr > F
Regression	4	78560	19640	149.0	0.000
Residual Error	89	11720	132.0		
Total	93	90280			

R-Square(adj) = 84.6%

Table 5 Parameter Test of Piecewise 2nd-order Model Valid for $d < 0$.

Predictor	Parameter Estimate	Standard Error	t value	Pr > [t]
Constant	90.3	2.24	40.4	0.000
Distance	280	17.9	15.6	0.000
(Sample Type) ²	-1.71	0.249	-6.88	0.000
Distance*Thickness	-65.6	13.4	-4.91	0.000
Thickness*Sample Type	17.7	2.42	7.32	0.000

Equations 4.3 and 4.4 show the fitted equations for a piecewise model of spatial light propagation ($\lambda = 830$ nm) through brain tissue at various thicknesses. Both models are second order polynomials based on horizontal distance from the receiving fiber, tissue thickness, and the interaction between the two variables. The analysis of variance for the

spatial light propagation model with $x_1 \geq 0$ is shown in Table 6. Table 7 shows the parameter estimates for the same model. The important terms for this model were the first order distance and thickness terms and the second order thickness term.

$$y = 62.7 - 257x_1 + 95.0x_2 - 41.8x_2^2, \quad x_1 \geq 0 \quad \text{Equation 4.3}$$

$$y = 70.5 + 352x_1 + 98.9x_2 - 52.2x_2^2 - 138x_1x_2, \quad x_1 < 0 \quad \text{Equation 4.4}$$

Table 6 ANOVA for the Spatial Light Propagation Data for $x_1 \geq 0$.

Analysis of Variance					
Source	Degrees of Freedom	Sum of Squares	Mean Square	F value	Pr > F
Regression	3	47566	15855	131.8	0.000
Residual Error	44	5293	120		
Total	47	52859			

$$R\text{-Square}(\text{adj}) = 89.3\%$$

Table 7 Parameter Testing for the Spatial Light Propagation Data Model Fit for $x_1 \geq 0$.

Predictor	Parameter Estimate	Standard Error	t value	Pr > [t]
Constant	62.7	7.21	8.70	0.000
Distance	-257	13.6	-18.9	0.000
Thickness	95.0	18.0	5.29	0.000
Thickness ²	-41.8	10.1	-4.16	0.000

Table 8 shows the analysis of variance for the spatial light propagation model with $x_1 < 0$. Table 9 shows the parameter estimates for the model. The negative model has the same significant terms as the positive piecewise model but includes an interaction term between the distance and sample thickness terms. The interaction term for the positive model was at the borderline for being significant with the p-value = 0.055. The

term was left out of the positive model because the ability of the model to predict transmission for new data was 4.6% higher without the interaction term.

Table 8 ANOVA for the Spatial Light Propagation Data for $x_1 < 0$.

Analysis of Variance					
Source	Degrees of Freedom	Sum of Squares	Mean Square	F value	Pr > F
Regression	4	44445	11111	138.81	0.000
Residual Error	46	3682	80		
Total	50	48127			

R-Square(adj) = 91.7%

Table 9 Parameter Testing for the Spatial Light Propagation Data Model Fit for $x_1 < 0$.

Predictor	Parameter Estimate	Standard Error	t value	Pr > [t]
Constant	70.45	6.74	10.45	0.000
Distance	352.23	26.84	13.12	0.000
Thickness	98.94	15.62	6.33	0.000
Thickness ²	-52.16	8.91	-5.85	0.000
Distance*Thickness	-137.97	21.38	-6.45	0.000

Figure 45 shows the model's prediction of the percent of light transmitted through brain tissue at various thicknesses as the source fiber is moved incrementally from the receiving fiber. As in the experimental data, the effect of scattering increases with the sample thickness. Figure 46 compares the experimental data to the model prediction for a sample thickness of 0.5 mm. For thicknesses greater than 0.5 mm, the model tends to overestimate the amount of transmitted light when the source fiber is centered with the receiving fiber. The quantity of transmitted light at the center of each sample was normalized to 100%, but the model was unable to accommodate different sample thicknesses having the same transmission intensity. It may be possible to correct

this by including an intensity term in the model or predicting the relative intensity of the transmitted light rather than the percent of transmitted light.

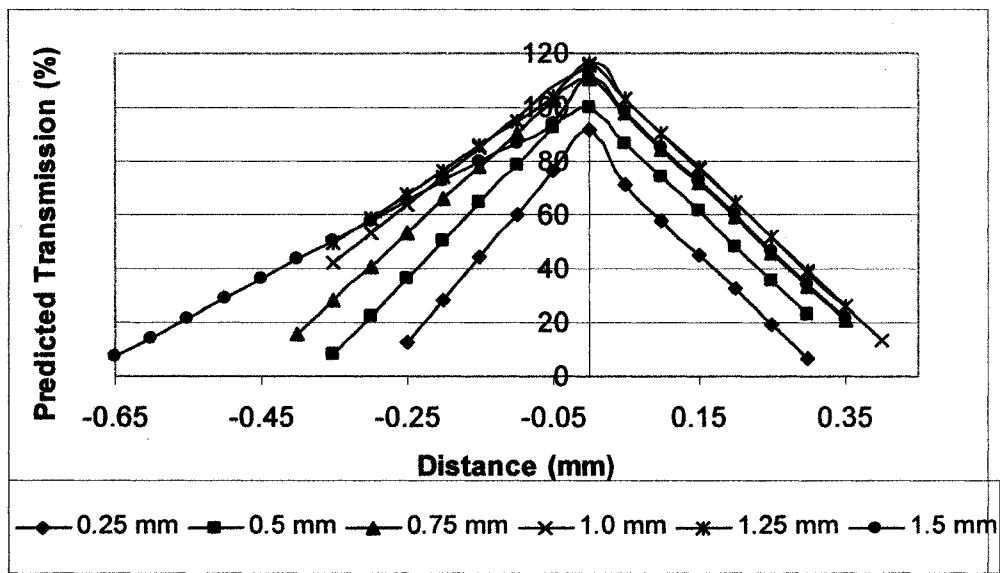


Figure 45 The predicted transmission at $\lambda = 830$ nm through brain tissue for the spatial propagation model.

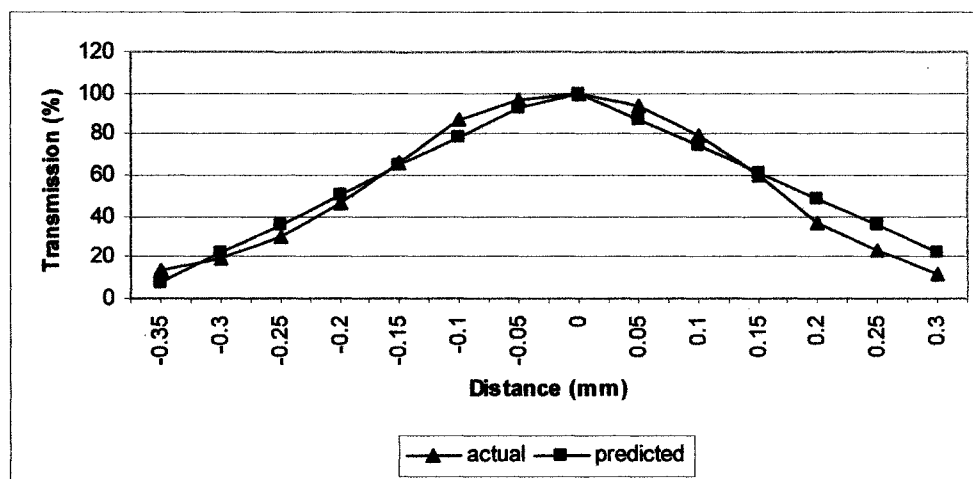


Figure 46 Comparison of the experimental data to the predicted transmission for the spatial propagation model at $\lambda = 830$ nm at a tissue thickness of 0.5 mm.

CHAPTER 5

DISCUSSION

5.1 Volume Conductor Response of Photodiodes

The voltage generated on the surface of the photodiode contact is the same for all diode geometries and contact materials. This is expected due to the shared interior design of all diode geometries. The voltage recording on the contact surface does not change as the recording electrode is moved across the surface of the contact. For the recordings made in the volume conductor, the positioning of the recording electrode becomes very important due to the uneven current density of the contacts. The current density is lowest at the center of the contact and rises sharply near the edge of the contacts. The voltage measurements studied in this work were taken at the center of the contact, but there may be some error in the measurements due to human error in the electrode positioning from diode to diode. This error comes from the difficulty of securing each diode into the volume conductor setup and centering the recording electrode over the cathode.

Figures 23-29 demonstrate that the amount of charge transferred into the volume conductor is dependent on the contact material. For IrOx, the charge injection rate was 0.3474 mC/cm^2 , which is much lower than the 3 mC/cm^2 rate for activated IrOx reported in the literature [39]. The rate we saw is similar to the limits of up to 0.5 mC/cm^2 of non-activated sputtered IrOx [43]. The low rate of charge injection and the primarily capacitive charge transfer indicate a flawed activation process for the sputtered IrOx. The

response of the IrOx photodiode in the Peachey and Chow study shows a much more faradic response and behaves like activated IrOx [25]. The PW in this study is 100 ms instead of the 200 μ s used here. However, the length of the pulse should not affect the voltage elevation at the end of the post. The deposition method used by Peachey and Chow is not described, but an alternative deposition of the IrOx may improve the response of these photodiodes.

The activation process consisted of using cyclic voltammetry to build up a multilayer film of IrOx. An electrode connected the cathode contact to the three electrode configuration for the cyclic voltammetry, and a film appeared to form on the cathode contact but not on the anode contact. The IrOx film on the cathode had a hole where the electrode touched the contact. If the setup was reversed to run current through the anode, the anode acquired a film but the film on the cathode contact was reduced. Because the injected charge density was less than the 0.5 mC/cm² needed for stimulation [52-55], the IrOx coated diodes were not used in *in vivo* testing.

The charge injection rate for the platinized photodiodes was 0.939 mC/cm², 2.3 times the 400 μ C/cm² reported limits for safe stimulation with Pt [36]. During testing, evidence of gassing was observed above the cathode in the form of small bubbles. It is possible to lower this charge injection rate by decreasing the platinization time to limit the amount of Pt black deposited on the contacts. However, the extreme sensitivity of the Pt black to mechanical friction makes implantation of these photodiodes difficult. Due to the inevitable threat of mechanical damage and of the rapid response decay with pulsing, the Pt black diodes were not used for the *in vivo* experiments.

After investigating IrOx and Pt, three TiN coated photodiode types were chosen for the *in vivo* experiments: diodes 15, 18, and 19. The charge injection rates for these photodiodes were 1.12 mC/cm^2 , 0.54 mC/cm^2 , and 1.43 mC/cm^2 . The wide range of charge densities is possibly due to the partially successful lift-off process. The lift-off process works best if the photoresist layer is substantially thicker than the metal layer deposited over the photoresist [56]. For very thick coatings, it is possible for the unwanted metal to form too strong a bond to the desired metal pattern. Even though the photoresist is dissolved, a layer of metal may remain in undesirable areas. A higher ratio of photoresist thickness to metal thickness may allow more leverage during the lift-off process, allowing a more complete removal of unwanted metal. The $1 \text{ }\mu\text{m}$ thickness of the photoresist was less than twice the thickness of the 635 nm TiN layer. This led to an uneven lift-off across the photodiode wafer, with diodes in the center receiving little to no lift-off. Multiple diodes of the same geometry taken from one corner of the wafer have comparable waveforms and peak voltages. One method to correct the lift-off problem for future diodes is to increase the thickness of the photoresist layer. Current techniques allow a photoresist thickness of up to $2.5 \text{ }\mu\text{m}$, and researchers are exploring the use of special photoresist materials allowing thicknesses of over $60 \text{ }\mu\text{m}$ [57].

It may also be possible to use a thinner layer of TiN by roughing the surface of the Au contact before TiN deposition to increase the eventual real surface area of the contact. The TiN coated microphotodiodes designed by Schlosshauer et al. have a similar response to the ones tested in this study [26]. The thickness of the TiN layer used in the microphotodiode arrays is a much thinner than the 635 nm layer, which prevented the

lift-off problems. It may be possible to significantly decrease the thickness of the TiN coating and maintain the charge generation needed for stimulation.

The voltage fields generated in the volume conductor above the cathode of a Pt black coated photodiode are shown in Figure 47. The voltage measurements are shown at $z = 0, 20,$ and $40 \mu\text{m}$, with $0 \mu\text{m}$ defined as just above the surface of the contact. The signal amplitude decreases with increasing distance from the surface. The voltage generated in the volume conductor drops to 70% at $20 \mu\text{m}$ and to 50% at $40 \mu\text{m}$. This rapid decrease of voltage indicates that the diodes will only stimulate the neurons a short distance from the photodiode.

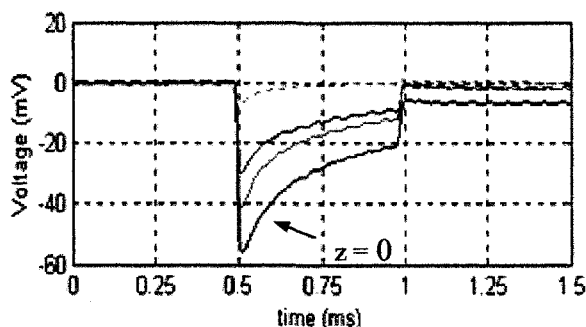


Figure 47 Volume conductor voltage measurements at $z = 0, 20,$ and $40 \mu\text{m}$ above the cathode of a Pt photodiode.

In Figure 48 a train of four pulses is applied to the Pt coated photodiode and the voltage potentials are recorded both directly from the cathode by touching with the tip of the recordings electrode and immediately above the surface. The waveform between the pulses indicates an incomplete discharging of the interface. In the recordings just above the surface, the peak of the first pulse is similar to what was observed in the single pulse stimulation. However, the voltage peak decreases with each successive pulse. In the case of a high frequency pulse train, the interface cannot discharge sufficiently between the

pulses, and the amplitude injected into the volume decays continuously with each additional pulse. The time constant of 17.3 ms places a conservative limit of ~ 57 Hz as the maximum frequency of stimulation. This frequency cap would allow for peripheral nerve stimulation and DBS at the 25-50 Hz frequencies needed in the periventricular gray matter and the primary motor cortex [5, 58]. However, stimulation in the subthalamic nucleus and the thalamic ventrointermediate nucleus require frequencies of 100-180 Hz, which would be out of the stimulation frequency range determined in our experiments with the diodes [59-61]. A potential solution to this problem is to incorporate a parallel resistance into the device that reduces the time constant, although this would also shunt some of the stimulation current.

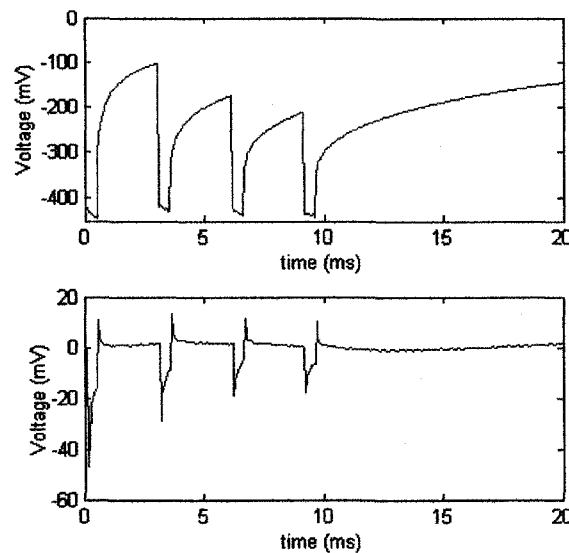


Figure 48 Pulse train measurements of a Pt diode with the recording electrode A) touching the contact and B) just above the surface of the contact at $z = 0 \mu\text{m}$.

5.2 EMG Response to Microphotodiodes

The EMG response to the frequency stimulation of the implanted photodiodes follows the normal pattern of frequency summation with individual contractions at low

frequencies and tetanization occurring at frequencies above 40 Hz [62]. The orientation of the photodiode with respect to the nerve fiber is essential to the success of stimulation. The diode must lie parallel to the nerve fiber to stimulate the nerve which increases the difficulty of implantation. This problem arises in implantation in the spinal cord, but the effect on diodes implanted in the brain is not as clear. The need for very specific implant position may require a change in the implantation method envisioned for the CNS. The proposed implantation method for the CNS used a needle to inject the diode at the desired location, but the final orientation of the diode is challenging to control. A potential solution to this problem is to move the anode to cover the underside of the device, as in the microphotodiode arrays designed by Schlosshauer et al. [26]. This move would increase the number of nerve fibers touched by the anode, and stimulation would be less dependent on the positioning of the diode. The size of the AA and cathode could also be increased even as the overall length of the device is decreased.

Peripheral implants present the difficulty of maintaining the diode position during muscle movement caused by stimulation. The shifting during stimulation causes increases in laser threshold power and minimum pulse widths. Although muscle movement is not an issue with implants into the brain, micromotion may cause similar problems. A potential solution is to use a laser beam diameter larger than the active area to compensate for shifts in the implant position with respect to the skull.

5.3 In Vivo Laser Power Threshold

Diode type 15 (AA = 10,000 μm^2 , CA = 12,000 μm^2) had a much higher charge density than diode type 18 (AA = 40,000 μm^2 , CA = 12,000 μm^2) but was not successful in achieving nerve stimulation. Diode type 18 had an active area 4 times larger than diode

15, which implies that the amount of light able to be transferred through the tissue into the diode is more significant than the charge density of the contacts. Diode type 19 (AA = $40,000 \mu\text{m}^2$, CA = $28,750 \mu\text{m}^2$) and diode type 18 had the same size active area, but diode type 19 had a larger contact area and higher charge density. While diode type 18 and diode type 19 had different charge densities, differences in stimulation thresholds were insignificant for longer pulse widths and for shallow implantation depths. However, for deeper depth stimulations or for shorter pulse width stimulations, differences in the charge density became more important. Diode type 18 required more laser power for pulse widths less than $50 \mu\text{s}$ which became more pronounced as implant depth increased. The model developed in Equation 4.2 shows that the indicator variable of diode type only contributes to the model as it interacts with the depth variable. This interaction implies that the diode type becomes more significant as the implant depth increases. Figure 40 confirms the higher stimulation threshold needed for diode 18 at implant depths greater than 2.5 mm.

The method used to measure the thickness of a tested nerve fiber flattened the fiber to fit a specific thickness. Although care was taken to allow adequate space for lateral deformation of the nerve fibers, the density of the fibers within the nerve may have been increased. Increased density could lead to decreased transmission due to higher scattering. If this is the case, a photodiode implanted into a free nerve may have a deeper maximum implant depth than the diodes tested in this work.

While these experiments revealed that diode type becomes more important with increasing implantation depth, the experiments did not answer the question of whether the power threshold differences between diodes 18 and 19 were due to the size of the

contact area or the difference in charge density. Future *in vivo* experiments need to include diodes 18 and 19 with similar charge densities to discover if the charge density or the different contact area size is the factor affecting the power threshold. If the stimulation threshold is different for each type of diode while the charge densities of diode types 18 and 19 are the same, then the factor will be the size of contact area.

Figure 35 and 36 show that the power stimulation thresholds of both diodes are steady for pulse widths greater than 50 μs with implantation depth less than 2.5 mm. This indicates that the charge generated in the first 50 μs of the pulse is largely responsible for the nerve stimulation. The charge in this portion of the pulse comes significantly from the capacitive peak which can be improved with the methods discussed in section 5.1. The reliance on capacitive transfer is encouraging for the success of TiN as the contact material for the microphotodiodes. Figure 39 shows the optimum pulse widths for 2.5 mm and 3.5 mm implantation depths are 40 μs and 60 μs . At the minimum pulse width for a depth of 3.5 mm, the energy required for stimulation is 0.53 mJ/cm^2 , which is 30 times lower than the maximum permissible exposure (MPE) of 16 mJ/cm^2 for $\lambda = 830$ nm with total exposure of $3 \times 10^4 \text{ s}^1$ [63]. Although both the minimum and optimum pulse widths indicate that the diodes could be used to stimulate deeper implants, this was not possible in these *in vivo* experiments.

The successful stimulation with diode 18, with a small contact area, was encouraging for the possibility of minimizing the photodiode size. Adjusting the low charge density of 0.54 mC/cm^2 to $\sim 1 \text{ mC}/\text{cm}^2$ (as discussed in section 5.1) may improve the diode's performance without increasing the overall size. While adjusting the charge

density of the diode may improve performance, the size of the AA was of vital importance in stimulating the nerve tissue and may be the limiting factor in determining the minimum size of the microphotodiodes. In contrast, for the Peachey and Chow microphotodiode array, the size of the AA is $8 \times 8 \mu\text{m}^2$, the same as that of the contact area [25]. This AA is much smaller than the ones discussed in this work, but is able to generate more than sufficient current for stimulation. However, the array is implanted into the retina, which is designed to allow light to pass. Because of its location, the light attenuation is much lower for the arrays than for the single photodiode. In addition, the anode is 2 mm in diameter, much larger than the contact size for the floating microstimulators discussed here. The large size decreases the overall resistance which increases the current generated by the device.

5.4 NIR Light Propagation

The NIR light spatial propagation experiments were used to determine the minimum separation needed for individual stimulation in implanted photodiodes. Due to equipment limitations, the maximum tissue thickness investigated was 1.5 mm, 2 mm less than the thickness used in the *in vivo* experiments. Because the 50 mW laser used for the *in vivo* experiments saturated the SD2000 spectrometer even when filtered to reduce the intensity, the FO-6000 tungsten light source which was only capable of penetrating 1.5 mm of brain tissue was used in the propagation experiments. Future experiments should employ a light source capable of penetrating 5 mm without saturating the spectrometer. However, these initial experiments show that as penetration depth increases so does the beam diameter; this increase in beam diameter is due to light scattering.

At a penetration depth of 0.5 mm, 95% of the light intensity is transmitted through the tissue when measured at a 50 μm radius from the center of the beam (Figure 43). The percent of transmitted light gradually decreased outside of this radius. At the 1.0 mm penetration depth, a wide plateau of over 95% intensity developed, followed by a much more rapid loss of intensity outside of the 150 μm radius as measured from the center of the beam. As the tissue thickness increased, the area covered by the penetrating light increased. Given the 200 μm by 200 μm AA required for stimulation (as mentioned in Section 5.3), a full intensity beam with 300 μm diameter centered over one diode is unlikely to stimulate a second diode.

The model developed in Equations 4.3 and 4.4 and shown in Figure 45 did not accurately reflect the plateau of 95% light transmission observed at tissue thickness of at least 1.0 mm, and instead, the model overestimates the percent of light transmitted in this region around the receiving fiber. However, the model predicted the rapid decrease of transmitted light outside of the plateau region for these tissue thicknesses. For an implantation depth of 1.5 mm, the model predicted a minimum separation distance (defined as the distance between the center of one diode active area to the center of the other diode active area) to be 428 μm when the two implants are stimulated at the optimum PW. Two 500 μm long diodes could be implanted lengthwise end to end and still be stimulated with separate beams, but the 300 μm width diodes implanted widthwise would need to be 128 μm apart to be stimulated by separate beams.

CHAPTER 6

CONCLUSIONS AND FUTURE WORK

The best contact material for use on the photodiodes studied in this work was TiN due to its mechanical stability and lasting charge density sufficient to achieve stimulation. The use of alternate microfabrication techniques for deposition of the TiN should equalize the charge density across diode types. Due to the conflicting reports of the safety of TiN, a study of the long term biocompatibility of the photodiodes is needed. The recession of the contacts into the photodiode may improve the uniformity of charge density and reduce the chance of cell necrosis from spikes of charge density near the edge of the contact. Activation methods for IrOx are unsuccessful for the photodiode, preventing IrOx from being a valid choice for contact material. The mechanical instability and rapid loss of charge density prevent Pt black from being a successful contact material.

The change in the waveform, from $z = 0 \mu\text{m}$ to $z = 10 \mu\text{m}$, shows that only a part of the voltage generated by the diode is transferred into the medium surrounding the diode. The capacitive component of the interface is responsible for the majority of the charge transfer into the tissue. The rapid decay of the voltage as the electrode is moved away from the contact indicates that stimulation will only occur in tissue near the surface of the diode. The inability of the diode to rapidly discharge at higher frequencies limits

the usefulness of the photodiodes in DBS. Future experiments are needed to study the effect of a parallel resistance between the contacts to decrease the time needed for discharge.

An EMG response occurring as a result of laser stimulation of a microphotodiode implanted in the rat sciatic nerve is shown. To our knowledge, this is the first report, outside of the optic system, demonstrating direct evidence that neural stimulation using optically powered photodiodes is feasible. The orientation of the diode with respect to the nerve is vital to achieve stimulation. The success of stimulation in the PNS is encouraging for the chances of success in the CNS. The resistivity of the gray matter in the brain and the resistivity of the peripheral nerves are very similar, but the higher resistivity of the spinal cord requires higher current thresholds and may impede stimulation.

The energy required for stimulation increases as implantation depth increases. The energy required at the maximum tissue thickness is 30 times less than the maximum permissible exposure, indicating the possibility of deeper implantations without exceeding the safety threshold for NIR laser stimulation. The trend indicates that the energy required for stimulation occurs in the early part of the pulse and excess energy is transferred in longer pulses. This suggests that the capacitive component of the diode is responsible for stimulation. The size of the AA is the significant factor in determining the success of stimulation. Contact area size may be reduced to reduce device size as long as the charge density is maintained. Future work is needed to minimize the size of the device and determine the maximum implantation depth for stimulation.

The beam diameter of the NIR light increases due to scattering as it travels through the tissue. Despite the large increase in beam diameter, the stimulation of a neighboring diode is doubtful due to the apparent need for the entire AA to be exposed to the laser to convert enough energy to achieve stimulation. Future work is needed to determine the scattering effect of a tissue thickness of 5.0 mm.

The successful PNS stimulation at a 3.5 mm implantation depth at 30 times less than the maximum permissible exposure is an encouraging sign for the success of deeper implants. The similarity of the specific resistivity of the PNS and the grey matter of the CNS points to successful stimulation in the CNS. Because the devices are sensitive to small changes in device position caused by muscle movement, the future use of these devices is likely to be in the CNS. If CNS stimulation can be achieved at a depth of at least 5.0 mm, the microphotodiodes could be used in DBS of the primary motor cortex. Determining the minimum separation distance for single diode stimulation is crucial to discovering the number of devices that can be implanted.

APPENDIX A

CALCULATIONS FOR NIR SAFETY LIMITS

Maximum Permissible Exposure (MPE) Calculation for Skin Exposure [63]:

The following calculations are to show that the laser used in this model is under acceptable limits for the published safety standards for skin exposure in the NIR region.

For an exposure time of 50 μs in the wavelength region 700 to 1050 nm, Equation A.1 shows the formula used to calculate the MPE for values for skin is:

$$1.1 \times 10^{4+0.002\left(\frac{\lambda}{10^{-9}}-750\right)} \times t^{\frac{1}{4}} \quad \text{Equation A.1}$$

Because this model uses a repetitively pulsed laser instead of a continuous beam, two further criteria must be taken into account. The criterion that gives the most restrictive MPE is chosen. The criteria are:

Criterion 1

The exposure of any single pulse within a pulse train shall not exceed the MPE for a single pulse multiplied by a correction factor, $N^{-1/4}$, where N is the number of pulses in the exposure.

Criterion 2

The average exposure of a pulse train with duration τ shall not exceed the MPE for a single pulse of duration t_{pulse} .

Table 10 Symbols and Values used in NIR Safety Limit Calculation.

Quantity	Symbol	Value
laser pulse duration	t_{pulse}	50 μs
number of pulses	N	100
total exposure duration	T	0.005 s
Wavelength	Λ	850 nm

Criterion 1, using $t = t_{\text{pulse}}$:

$$1.1 \times 10^{4+0.002(850-700)} \times 0.00005^{0.25} \times 100^{\frac{1}{4}} = 583.63 \frac{J}{m^2}$$

Criterion 2, using $t = \tau$:

$$1.1 \times 10^{4+0.002(850-700)} \times 0.005^{0.25} \div 100 = 58.36 \frac{J}{m^2}$$

Because criterion 2 is more restrictive, the MPE for this model at is 58.36 J/m².

APPENDIX B

PUBLICATIONS AND PRESENTATIONS

1. K. Gray, "Floating Light Activated Micro-Electrical Stimulators," *Biomedical Research Symposium at Louisiana Tech*, May 6, 2005.
2. K. Gray, S.A. Suvari, and M. Sahin, "Floating Light Activated Micro-Electrical Stimulators", *Neural Interfaces Workshop*, NIH and NINDS, November 16, 2004, Student Fellowship Awardee.
3. K. Gray, M. Sahin, S. Menn, and M. S. Unlu, "Neural Stimulation with a Floating Micro-Electrode," *BMES Annual Fall Meeting*, October 13, 2004.
4. K. Gray and M. Sahin, "Voltage Field Generated by a Single Photodiode in a Volume Conductor," Louisiana Tech University, *CyBERS SIG Meeting*, Oct 4, 2004.
5. H. K. Innamuri, K. Gray, and M. Sahin, "Finite Element Modeling of a Floating Micro-Stimulator," *BMES Annual Fall Meeting*, October 3, 2003.
6. K. Gray, H.K. Innamuri, A. Tayebi, and M. Sahin, "Voltage Field Generated by a Single Photodiode in a Volume Conductor: Simulation and Measurements," *25th Annual International Meeting of IEEE/Engineering in Medicine and Biology Society*, Cancun, Mexico, Sep 17-21, 2003.

REFERENCES

- [1] M. Y. Oh, A. Abosch, S. H. Kim, A. E. Lang, and A. M. Lozano, "Long-term hardware-related complications of deep brain stimulation," *Neurosurgery*, vol. 50, no. 6, pp. 1268-1274, June 2002.
- [2] A. L. Benabid, P. Pollak, A. Louveau, S. Henry, and J. de Rougemont, "Combined (thalamotomy and stimulation) stereotactic surgery of the VIM thalamic nucleus for bilateral Parkinson disease," *Applied Neurophysiology*, vol. 50, no. 1-6, pp.344-346, 1987.
- [3] D. Kondziolka, D. Whiting, A. Germanwala, and M. Oh, "Hardware-related complications after placement of thalamic deep brain stimulator systems," *Stereotactic and Functional Neurosurgery*, vol. 79, no. 3-4, pp. 228-233, 2002.
- [4] R. M. Levy, S. Lamb, and J. E. Adams, "Treatment of chronic pain by deep brain stimulation: Long term follow-up and review of the literature," *Neurosurgery*, vol. 21, no. 6, pp. 885-893, December 1987.
- [5] K. Kumar, C. Toth, and R. K. Nath, "Deep brain stimulation for intractable pain: A 15-year experience," *Neurosurgery*, vol. 40, no. 4, pp. 736-747, April 1997.
- [6] J. Voges et al., "Deep-brain stimulation: Long-term analysis of complications caused by hardware and surgery--experiences from a single centre," *Journal of Neurology, Neurosurgery, and Psychiatry*, vol. 77, no. 7, pp. 868-872, July 2006.
- [7] C. Joint, D. Nandi, S. Parkin, R. Gregory, and T. Aziz, "Hardware-related problems of deep brain stimulation," *Movement Disorders: Official Journal of the Movement Disorder Society*, vol. 17, no. S3, pp. S175-S180, 2002.
- [8] P. Blomstedt and M. I. Hariz, "Hardware-related complications of deep brain stimulation: A ten year experience," *Acta Neurochirurgica*, vol. 147, no. 10, pp. 1061-1064, October 2005.
- [9] A. Beric et al., "Complications of deep brain stimulation surgery," *Stereotactic and Functional Neurosurgery*, vol. 77, no. 1-4, pp. 73-78, 2001.

- [10] M. J. Wiggins, B. Wilkoff, J. M. Anderson, and A. Hiltner, "Biodegradation of polyether polyurethane inner insulation in bipolar pacemaker leads," *Journal of Biomedical Materials Research*, vol. 51, no. 8, pp. 302-307, May 2001.
- [11] G. Pearson, W. T. Read, and W. L. Feldman, "Deformation and fracture of small silicon crystals," *Acta Metallurgica*, vol. 5, pp. 181-191, 1957.
- [12] J. U. Meyer, D. J. Edell, W. L. C. Rutten, and J. Pine, "Chronically implantable neural information transducers," *Proceedings-18th Annual Conference-IEEE/EMBS*, pp. 2139-2141, 1996.
- [13] J. Muthuswamy, R. Saha, and A. Gilletti, "Tissue micromotion induced stress around brain implants," *Proceedings-3rd Annual Conference-IEEE/EMBS on Microtechnology*, pp. 102-103, May 2005.
- [14] J. Subbaroyan, D. C. Martin, and D. R. Kipke, "A finite-element model of the mechanical effects of implantable microelectrodes in the cerebral cortex," *Journal of Neural Engineering*, vol. 2, no. 4, pp. 103-113, December 2005.
- [15] D. B. Popovic, "Functional electrical stimulation for lower extremities," in *Neural Prostheses: Replacing Motor Function after Disease or Disability*, R. B. Stein, P. H. Peckham, and D. B. Popovic, Eds. Oxford: Oxford University Press, pp. 233-251, 1992.
- [16] A. C. Hoogerwerf and K. D. Wise, "A 3-dimensional microelectrode array for chronic neural recording," *IEEE Transactions on Biomedical Engineering*, vol. 41, pp. 1136-1146, 1994.
- [17] D. J. Edell, V. V. Toi, V. M. McNeil, and L. D. Clark, "Factors influencing the biocompatibility of insertable silicon microshafts in cerebral cortex," *IEEE Transactions on Biomedical Engineering*, vol. 39, pp. 635-643, 1992.
- [18] J. F. Hetke, J. L. Lund, and K. Najafi, "Silicon cable ribbons for chronically implantable microelectrode arrays" *IEEE Transactions on Biomedical Engineering*, vol. 41, no. 4, pp. 314-321. April 1994.
- [19] G. E. Loeb, C. J. Zamin, J. H. Schulman, and P. R. Troyk, "Injectable microstimulator for functional electrical stimulation," *Medical & Biological Engineering & Computing*, vol. 29, no. 6, pp. S13-19, November 1991.
- [20] H. R. Eggert and V. Blazek, "Optical properties of human brain tissue, meninges, and brain tumors in the spectral range of 200 to 900 nm," *Neurosurgery*, vol. 21, no. 4, pp. 459-464, 1987.
- [21] A. J. Welch, "The thermal response of laser irradiated tissue," *IEEE Journal of Quantum Electronics*, vol. 20, no. 12, pp. 1471-1481, 1984.

- [22] G. Strangman, D. Boas, and J. P. Sutton, "Non-invasive neuroimaging using near-infrared light," *Biological Psychiatry*, vol. 52, no. 7, pp. 679-693, 2002.
- [23] A. Y. Chow et al., "Implantation of silicon chip microphotodiode arrays into the cat subretinal space" *IEEE Transactions on Neural Systems and Rehabilitation Engineering*, vol. 9, pp. 86-95, 2001.
- [24] G. Peyman, A. Y. Chow, C. Liang, V. Y. Chow, J. I. Perlman, and N. S. Peachey, "Subretinal semiconductor microphotodiode array," *Ophthalmic Surgery and Lasers*, vol. 29, no. 3, pp.234-241, 1998.
- [25] N. S. Peachey and A. Y. Chow, "Subretinal implantation of semiconductor-based photodiodes: Progress and challenges," *Journal of Rehabilitation Research and Development*, vol. 36, no. 4, pp. 371-376, October 1999.
- [26] B. Schlosshauer, A. Hoff, E. Guenther, E. Zrenner, and H. Hammerle, "Towards a retina prosthesis model: Neurons on microphotodiode arrays in vitro," *Biomedical Microdevices*, vol. 2, no. 1, pp. 61-72, 1999.
- [27] E. Zrenner et al., "Can subretinal microphotodiodes successfully replace degenerated photoreceptors?" *Vision Research*, vol. 39, pp. 2555-2567, 1999.
- [28] J. G. Webster, Ed. *Medical Instrumentation: Application and Design*. 3rd ed., New York: John Wiley and Sons, Inc, 1998.
- [29] D. R. Merrill, M. Bikson, and J. G. R. Jefferys, "Electrical stimulation of excitable tissue: Design of efficacious and safe protocols," *Journal of Neuroscience Methods*, vol. 141, pp. 171-198, 2004.
- [30] T. Ragheb and L. A. Geddes, "Electrical properties of metallic electrodes," *Medical & Biological Engineering & Computing*, vol. 28, pp. 182-186, 1990.
- [31] S. Mayer, L. A. Geddes, J. D. Bourland, and L. Ogborn, "Faradic resistance of the electrode/electrolyte interface," *Medical & Biological Engineering & Computing*, vol. 30, pp. 538-542, 1992.
- [32] A. Blau et al., "Characterization and optimization of microelectrode arrays for *in vivo* nerve signal recording and stimulation" *Biosensors & Bioelectronics*, vol. 12, no. 9-10, pp. 883-892, 1997.
- [33] H. P. Schwan, "Alternating Current Electrode Polarization," *Biophysik*, vol. 3, pp. 181-201, 1966.

- [34] D. B. McCreery, W. F. Agnew, T. G. H. Yuen, and L. Bullara, "Charge density and charge per phase as cofactors in neural injury induced by electrical stimulation," *IEEE Transactions on Biomedical Engineering*, vol. 37, pp. 996-1001, October 1990.
- [35] S. F. Cogan, P. R. Troyk, J. Ehrlich, T. D. Plante, and D. E. Detlefsen, "Potential-biased, asymmetric waveforms for charge-injection with activated iridium oxide (AIROF) neural stimulation electrodes," *IEEE Transactions on Biomedical Engineering*, vol. 53, no. 2, pp.3270332, February 2006.
- [36] S. B. Brummer, L. S. Robblee, and F. T. Hambrecht, "Criteria for selecting electrodes for electrical stimulation: Theoretical and practical considerations," *Annals of the New York Academy of Sciences*, vol. 405, pp. 159-171, 1983.
- [37] R. S. Robblee, J. K. Lefko, and S. B. Brummer, "Activated iridium: An electrode suitable for reverse charge injection in saline solution," *Journal of the Electrochemical Society*, vol. 130, pp. 731-733, 1983.
- [38] W. F. Agnew, T. G. H. Yuen, D. B. McCreery, and L. A. Bullara, "Histopathologic evaluation of prolonged intracortical electrical stimulation," *Experimental Neurology*, vol. 92, pp. 162-185, 1986.
- [39] J. D. Weiland and D. J. Anderson, "Chronic neural stimulation with thin-film, iridium oxide electrodes," *IEEE Transactions on Biomedical Engineering*, vol. 47, no. 7, pp. 911-918, July 2000.
- [40] X. Beebe and T. L. Rose, "Charge injection limits of activated iridium oxide electrodes with 0.2 ms pulses in bicarbonate buffered saline," *IEEE Transactions on Biomedical Engineering*, vol. 35, no. 6, pp. 494-495, June 1988.
- [41] J. D. Weiland, D. J. Anderson, and M. S. Humayun, "In vitro electrical properties for iridium oxide versus titanium nitride stimulating electrodes," *IEEE Transactions on Biomedical Engineering*, vol. 49, no. 12, pp. 1574-1579, December 2002.
- [42] M. Schaldach, M. Hubmann, A. Wickl, and R. Hardt, "Sputter-deposited TiN electrode coatings for superior sensing and pacing performance," *Pacing and Clinical Electrophysiology*, vol. 13, pp. 181-193, 1990.
- [43] S. F. Cogan, "Microelectrode coatings for neural stimulation and recording," *Proceedings-25th Annual Conference-IEEE/EMBS*, pp. 3798-3801, 2003.
- [44] A. Norlin, J. Pan, and C. Leygraf, "Investigation of interfacial capacitance of Pt, Ti and TiN coated electrodes by electrochemical impedance spectroscopy," *Biomolecular Engineering*, vol. 19, pp. 67-71, 2002.

- [45] D. M. Zhou and R. J. Greenberg, "Electrochemical characterization of titanium nitride microelectrode arrays for charge-injection applications," *Proceedings-25th Annual Conference-IEEE/EMBS*, pp. 1964-1967, 2003.
- [46] H. Hammerle, K. Kobuch, K. Kohler, W. Nisch, H. Sachs, and M. Stelzle, "Biostability of micro-photodiode arrays for subretinal implantation," *Biomaterials*, vol. 23, pp. 797-804, 2002.
- [47] E. Guenther, B. Tröger, B. Schlosshauer, and E. Zrenner, "Long-term survival of retinal cell cultures on retinal implant materials," *Vision Research*, vol. 39, no. 24, pp. 3988-3994, December 1999.
- [48] A. Wilke, G. Schroder, J. Orth, P. Griss, and R. P. Franke, "Evaluation of the biocompatibility of implant materials with human bone marrow cell cultures," *Biomedizinische Technik. Biomedical engineering*, vol. 38, pp. 126-129, June 1993.
- [49] C. N. Sulkenik, N. Ballachander, L. A. Culp, K. Lewandowska, and K. Merritt, "Modulation of cell adhesion by modification of titanium surfaces with covalently attached self-assembled monolayers," *Journal of biomedical materials research*, vol. 24, no. 10, pp. 1307-1323, October 1990.
- [50] J. Haueisen, C. Ramon, P. Czapski, and M. Eiselt, "On the influence of volume currents and extended sources on neuromagnetic fields: A simulation study," *Annals of Biomedical Engineering*, vol. 23, no. 6, pp. 728-739, November-December, 1995.
- [51] C. Daniel and F. S. Wood, *Fitting Equations to Data*, 2nd ed., Wiley. New York. 1980.
- [52] E. M. Schmidt, M. J. Bak, F. T. Hambrecht, C. V. Kufta, D. K. O'Rourke, and P. Vallabhanath, "Feasibility of a visual prosthesis for the blind based on intracortical microstimulation of the visual cortex." *Brain: A Journal of Neurology*, vol. 119, pp. 507-522, 1996.
- [53] D. B. McCreery, L. A. Bullara, and W. F. Agnew, "Neuronal activity evoked by chronically implanted intracortical electrodes," *Experimental Neurology*, vol. 92, pp. 147-161, 1986.
- [54] D. B. McCreery, W. F. Agnew, and L. A. Bullara, "The effects of prolonged intracortical microstimulation of the excitability of pyramidal tract neurons in the cat," *Annals of Biomedical Engineering*, vol. 30, pp. 107-119, 2002.
- [55] W. M. Grill, N. Bhadra, and B. Wang, "Bladder and urethral pressures evoked by microstimulation of the sacral spinal cord in cats," *Brain Research*, vol. 836, pp. 19-30, 1999.

- [56] B. Y. Park, R. Zaouk, and M. J. Madou, "Fabrication of microelectrodes using the lift-off technique," *Microfluidic Techniques*, Shelley D. Minter, Ed. New Jersey: Humana Press, pp. 23-26, 2006.
- [57] P. Niedermann et al., "A novel thick photoresist for microsystem technology," *Microelectronic Engineering*, vol. 67, pp. 259-265, 2003.
- [58] S. Canavero et al., "Extradural motor cortex stimulation for advanced Parkinson's disease," *Journal of Neurosurgery*, vol. 97, pp. 1208-1211, 2002.
- [59] L. Capus et al., "Chronic bilateral electrical stimulation of the subthalamic nucleus for the treatment of advanced Parkinson's disease," *Neurological Sciences*, vol. 22, pp. 57-58, 2001.
- [60] B. Haslinger et al., "Differential modulation of subcortical target and cortex during deep brain stimulation," *NeuroImage*, vol. 18, pp. 517-524, 2003.
- [61] M. Rizzone et al., "High-frequency electrical stimulation of the subthalamic nucleus in Parkinson's disease: Kinetic and kinematic gait analysis," *Neurological Sciences*, vol. 23, pp. S103-104, 2002.
- [62] A. C. Guyton and J. E. Hall, *Textbook of Medical Physiology*, 10th ed., W. B. Saunders. Philadelphia. 2000.
- [63] American National Standards Institute. *Z136.1 Safe Use of Laser*. ANSI. 2007.